Kusari *et al. BMC Biology* (2025) 23:85
https://doi.org/10.1186/s12915-025-02167-1

BMC Biology

METHODOLOGY ARTICLE

Open Access

Label-free metabolic fingerprinting of motile mammalian spermatozoa with subcellular resolution

Fitore Kusari[1,2*], Lenka Backova[3,4,5], Dalibor Panek[3], Ales Benda[3] and Zdenek Trachtulec[1*]

Abstract

Background Sperm metabolic pathways that generate energy for motility are compartmentalized within the flagellum. Dysfunctions in metabolic compartments, namely mitochondrial respiration and glycolysis, can compromise motility and male fertility. Studying these compartments is thus required for fertility treatment. However, it is very challenging to capture images of metabolic compartments in motile spermatozoa because the fast beating of the flagellum introduces motion blur. Therefore, most approaches immobilize spermatozoa prior to imaging.

Results Our findings indicate that immobilizing sperm alters their metabolic profile, highlighting the necessity for measuring metabolism in spermatozoa during movement. We achieved this by encapsulating mouse epididymis in a hydrogel followed by two-photon fluorescence lifetime imaging microscopy for imaging motile sperm in situ. The autofluorescence of endogenous metabolites—FAD, NADH, and NADPH—enabled us to visualize sperm metabolic compartments without staining. We trained machine learning for automated image segmentation and generated metabolic fingerprints using object-based phasor analysis. We show that metabolic fingerprints of spermatozoa and the mitochondrial compartment (1) can distinguish individual males by genetic background, age, or fecundity status, (2) correlate with fertility, and (3) change with age likely due to increased oxidative metabolism.

Conclusions Our approach eliminates the need for sperm immobilization and labeling and captures the native state of sperm metabolism. This technique could be adapted for metabolism-based sperm selection for assisted reproduction.

Keywords FLIM, Sperm, Metabolism, NADH, NADPH, Fertility, Artificial intelligence

*Correspondence:
Fitore Kusari
fitore.kusari@mpinat.mpg.de
Zdenek Trachtulec
zdenek.trachtulec@img.cas.cz
[1] Laboratory of Germ Cell Development, Division BIOCEV, Institute of Molecular Genetics of the Czech Academy of Sciences, Prague, Czech Republic
[2] Present address: Department of Meiosis, Max Planck Institute for Multidisciplinary Sciences, Göttingen, Germany
[3] Imaging Methods Core Facility at BIOCEV, Faculty of Science, Charles University, Vestec, Czech Republic
[4] Present addresses: Instituto Biofisika CSIC, UPV/EHU, Leioa, Spain
[5] Department of Computer Science and Artificial Intelligence, University of Basque Country UPV/EHU, San Sebastián, Spain

Background

Mammalian spermatozoa compartmentalize metabolic reactions into distinct subcellular domains for efficient energy production [1]. Within the sperm flagellum, metabolic compartments are separated spatially and biochemically; mitochondrial oxidative phosphorylation (OXPHOS) localizes to the proximal segment of the flagellum (midpiece), and glycolysis confines to the more distal, yet longest flagellar segment (principal piece) [2, 3]. Glycolysis breaks down glucose to generate pyruvate, reduced nicotinamide adenine dinucleotide (NADH), and two molecules of adenosine triphosphate (ATP). Mitochondria oxidize metabolites, i.e., NADH

and pyruvate, to produce additional 34 molecules of ATP. Since mitochondria produce the bulk of ATP, it is argued that OXPHOS alone can meet spermatozoa's energy demands [4, 5]. This is true for dolphins [6], but mouse [7], rat [8], and human sperm [9, 10] rely on glycolysis in addition to OXPHOS to successfully move through the female reproductive tract and fertilize the egg. Consequently, metabolic dysfunction resulting from mutations in mitochondrial DNA [11–17] or in genes coding for sperm glycolytic enzymes [18–20] compromise motility and male fertility in mice and men. Understanding sperm subcellular metabolism is thus necessary for developing treatments: (i) to alleviate infertility due to metabolic dysfunction and (ii) for controlling fertility by inhibiting sperm-specific metabolic enzymes.

Spermatozoa provide a unique model to visualize compartmentalized metabolic processes, yet most studies measure the sperm metabolism using bulk assays. For example, magnetic resonance spectroscopy [21] and mass spectrometry [22, 23] technologies can catalog tens or hundreds of sperm metabolites, respectively. These bulk methods provide only averaged information on metabolites from all compartments and are thus unable to resolve spatiotemporal dynamic changes in metabolite levels or their distribution within the sperm. Imaging metabolites in different subcellular compartments of spermatozoa can therefore provide a unique view of bioenergetic processes without the limitations of population averages. However, metabolic imaging using exogenous labels as in fluorescence microscopy suffers from non-specific labeling, interference with native metabolic processes, and cytotoxicity [24]. To overcome these limitations, we sought to develop a method that: first, does not require adding or genetically encoding fluorophores; second, can measure compartmentalized metabolic pathways in spermatozoa; third, can be combined with machine learning tools for fast (semi)automated image analysis.

The autofluorescence of the metabolic cofactors: oxidized flavin adenine dinucleotide (FAD), reduced NADH and its phosphorylated analogue NADPH enables imaging of metabolism label-free in living cells [25]. The nicotinamide ring of NADH absorbs light at 340 (±30) nm and emits fluorescence at 460 (±50) nm [26]. Since NADPH is phosphorylated at a site away from the nicotinamide ring, the fluorescence properties of NADPH are identical to NADH [27]. As NADH and NADPH cannot be distinguished based on autofluorescence, the abbreviation NAD(P)H indicates the combined fluorescence signal [28]. In general, NAD(P)H within mitochondria is primarily bound to enzymes [29], whereas the unbound NAD(P)H freely diffuses in the cytosol and nucleus [30]. The free (unbound) and bound NAD(P)H were previously shown to reflect glycolysis and OXPHOS metabolism, respectively [31, 32]. Intensity-based imaging, however, cannot distinguish between the free and bound NAD(P)H due to their minor spectral differences [28]. Instead, we took advantage of the difference in fluorescence lifetime to measure the free and bound states. For instance, the lifetime of free NAD(P)H is short (~0.4 ns); however, upon enzymatic binding its lifetime increases to ~1.9–5.7 ns (depending on the enzyme bound) [30, 33]. Fluorescence lifetime is the average time a fluorophore takes in the excited state before returning to the ground state. Excited state fluorescence lifetime of a fluorophore is generally not influenced by fluorophore concentration and excitation intensity [34]. Therefore, images based on lifetime contrast are more suitable for quantitative analysis compared to fluorescence intensity images and can be compared between different systems and samples [35].

There are two strategies to measure fluorescence lifetime: time- and frequency-domain fluorescence lifetime imaging microscopy (FLIM) [36–38]. A pulsed or amplitude-modulated laser excites the sample for time- and frequency-domain FLIM, respectively. For time-domain, the fluorescence decay is measured using time-correlated single photon counting detection (TCSPC) or time-gated sensors, whereas the frequency-domain FLIM measures the relative changes in the amplitude and phase of the modulated fluorescence. Frequency-domain FLIM is implemented on widefield microscopes that are faster in acquisition speed but have lower spatial resolution compared to laser-scanning microscopes [38]. Although frequency-domain FLIM with UV excitation was used to measure NADH lifetime [39], images have low signal-to-noise ratio and are less reliable for lifetime quantification. Time-domain FLIM with TCSPC is more accurate than frequency-domain [37] and it is compatible with multiphoton excitation. This is important because two-photon (2P) near-infrared excitation FLIM bypasses the undesirable effects associated with near UV one-photon excitation for NAD(P)H imaging, such as cellular photodamage, photobleaching, and light scattering [40, 41]. Despite these advantages, rapid image acquisition is hindered by mechanical scanning and the maximum detection count rate, which is limited by the single-photon counting detectors' dead-time in TCSPC. Technological advances have sought to increase the acquisition speed of 2P-FLIM [42]. However, higher acquisition rates might affect the accuracy of the NAD(P)H lifetime measured [43], suggesting a trade-off between speed and sensitivity. Recently, light-sheet FLIM was developed for NAD(P)H imaging [44]. The acquisition speed per frame is faster than laser scanning 2P-FLIM, but compared to TCSPC, the detector array in light-sheet FLIM introduces artifacts that need correcting to ensure accuracy in lifetime

measurement [44]. While each method has both pros and cons, we chose 2P-FLIM with TCSPC for NAD(P)H imaging due to its high sensitivity, resolution, as well as low overall photo- and cytotoxicity.

Recent advances in image analysis using machine learning have surpassed human-level performance at image segmentation, revolutionizing the field of quantitative microscopy [45]. This makes machine learning a promising tool for automating tasks that previously could only be done by experts. We thus took advantage of machine learning for fast and precise segmentation of sperm subcellular structures from FLIM images.

Here, we introduce a 2P-FLIM-based framework for mapping the spatial distribution of endogenous metabolites within individual motile spermatozoa with subcellular resolution. We combined 2P-FLIM with machine learning and object-based phasor analysis [46] to generate sperm (sub)cellular metabolic fingerprints for mice of different genetic backgrounds, age, and fertility status.

Results and discussion

2P-FLIM reveals changes in NAD(P)H lifetimes within sperm induced by immobilization

Our method utilizes 2P-FLIM for imaging endogenous metabolites of sperm at the single-cell and subcellular levels. We chose 2P-FLIM because it is gentle to biological samples, uses endogenous contrast and provides high spatiotemporal resolution. 2P-FLIM was previously used to image NAD(P)H and FAD metabolites of immobile invertebrate spermatozoa [47, 48], and one-photon excitation FLIM was used for FAD imaging of immobilized human sperm [49]. The intracellular levels of FAD are lower compared to NAD(P)H, suggesting that FAD alone may not be a reliable metabolic marker [28, 50]. On the other hand, NAD(P)H alone has been previously utilized to monitor cellular metabolic changes [50–53]. However, the usage of 2P-FLIM for NAD(P)H imaging in mammalian sperm has not been demonstrated yet.

Imaging freely moving spermatozoa is technically challenging for two reasons: first, human [54], bull [55], rat, and mouse sperm swim near surfaces with circular or curvilinear trajectories [56]. As a result, parts of the flagellum are outside the focus plane of the microscope during live imaging. It is thus difficult to obtain the entire head and flagellum in one temporal frame. Second, spermatozoa swim very fast. In 1 s, the house mouse (*Mus musculus, M. m.*) sperm swim over an average distance of 105 µm [57]. Conventional NAD(P)H imaging by 2P-FLIM lacks the temporal resolution to capture sperm swimming. Although recent FLIM set-ups can acquire up to 25 frames per second (fps) [43], they are still too slow to capture mouse sperm swimming that requires about 50 fps [57]. To address the challenges of imaging motile sperm, we first tested immobilization of mouse sperm between coverslips in 1% LMPA. Immobilized spermatozoa were then imaged at 740 nm excitation to acquire the fluorescence intensity and lifetime of NAD(P)H (Fig. 1A). We noted that not all sperm compartments contributed equally to the signal. Mitochondria, found exclusively in the sperm midpiece, displayed a higher fluorescence intensity of NAD(P)H than the head and flagellar principal piece, both of which lack mitochondria (Fig. 1A). This is not surprising, since mitochondrial enzymes in the midpiece use NAD(P)H as cofactors. However, we observed an unexpected distribution of NAD(P)H lifetimes in subcellular compartments of immobilized sperm (Fig. 1A). Specifically, the lifetime of NAD(P)H in sperm mitochondria was shorter, indicating a higher ratio of free NAD(P)H, which is typically associated with glycolysis. On the other hand, the sperm head and principal piece compartments displayed longer NAD(P)H lifetimes (Fig. 1A), suggesting a higher ratio of bound NAD(P)H, typically found in mitochondria. This atypical metabolic profile within sperm compartments is also illustrated in phasor plots (Fig. 1B, C) that display NAD(P)H lifetimes graphically into a 2D coordinate plot (see "Methods") through object-based phasor analysis [58]. Contrary to NAD(P)H, FAD has a short lifetime when protein-bound, but a longer lifetime when it is free [59]. Both forms localize to mitochondria, as FAD serves exclusively as a cofactor for mitochondrial enzymes and it is not involved in glycolysis. We reasoned that 2P-FLIM measurements for FAD would be easier to interpret given that only mitochondria in the midpiece would fluoresce. To test this, we imaged FAD at 900 nm excitation in the same immobilized spermatozoa as for NAD(P)H. Although the intensity of FAD was brighter in midpiece compared to the head and principal piece (Fig. 1D), nearly identical lifetimes for FAD were observed within sperm compartments (Fig. 1E, F). While similar observations were made for immobilized human sperm [49], the fluorescence intensity and lifetime of FAD emanating from the head and principal piece was unexpected since both compartments lack mitochondria and rely on glycolysis. Such findings for NAD(P)H and FAD lifetimes contradict the conventional understanding of sperm metabolic compartments [60–62] and raise the possibility that our sample preparation or imaging set-up might influence the obtained data. To test the accuracy of the imaging set-up, we measured both free and bound NADH (NADH bound to LDH) [46] in solution. Our 2P-FLIM set-up distinguished between the free and bound-NADH (Additional file 1: Fig. S1), as shown by their distinct positions in the phasor plot, corresponding to their known lifetimes. These results rule out any imaging inaccuracies and suggest that sperm immobilization on coverslips

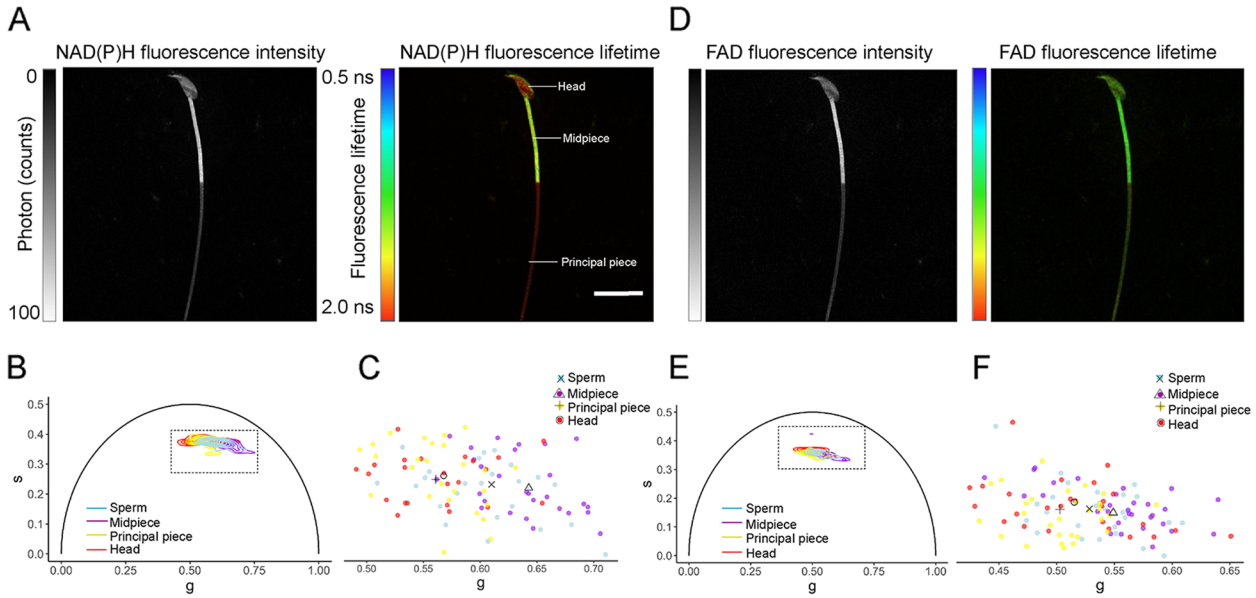

Fig. 1 2P-FLIM of immobilized sperm reveals atypical lifetimes for NAD(P)H and FAD within metabolic compartments. **A** Representative image of the fluorescence intensity (left) and lifetime (right) of NAD(P)H in immobilized sperm. Mitochondria in the midpiece showed increased intensity (indicative of higher NAD(P)H levels) compared to the dimmer head and flagellar principal piece. The excited state lifetime information is encoded into RGB-based FLIM images as a lookup table, with blue indicating short and red long average arrival times of photons after excitation. Note that mitochondria in the midpiece display shorter lifetimes of NAD(P)H, whereas the head and flagellar principal piece display longer lifetimes of NAD(P)H. **B** Object-based phasor plot of NAD(P)H and **C** the detailed view of individual points illustrate the metabolic state of individual immobilized spermatozoa and subcellular compartments including the midpiece, head, and principal piece. Means depicted as empty geometric shapes are plotted in the graph along the data points of individual sperm cells and subcellular compartments (filled shapes). **D** Representative images of the fluorescence intensity and lifetime of FAD. **E** Object-based phasor plot of FAD and **F** the detail view of individual points of immobilized spermatozoa and subcellular compartments including the midpiece, head, and principal piece. Scale bar, 20 µm

during sample preparation could skew the metabolic profile, possibly leading to unreliable results. We therefore sought to develop a sample preparation technique that does not require immobilization of spermatozoa to avoid perturbation of metabolic compartments.

NAD(P)H and FAD imaging using 2P-FLIM captures the native metabolism of motile sperm in situ

Since spermatozoa are normally confined in intact organs, we reasoned that live imaging of sperm in tissues might overcome the challenges when imaging these cells in suspension or immobilized on coverslips. In addition, the lack of imaging data on mammalian sperm metabolism within the native tissue environment further encouraged us to design a workflow for metabolic imaging of motile spermatozoa in situ (Additional file 2: Fig. S2).

In mammals, sperm acquire motility and fertilizing ability in the caudal (distal) part of the epididymis [63]. For this reason, cauda epididymis was selected as a model system for imaging. As model organisms we used house mice because of their similarity to humans in physiology and pathology [64]. To prepare the sample, freshly excised cauda epididymis was immersed in 1% LMPA hydrogel (see "Methods"). LMPA was chosen to encapsulate the sample in hydrogel to gently immobilize the tissue. Further, LMPA hydrogel encapsulation is rapid, inexpensive, has good optical properties, and is often used for imaging biological samples, i.e., mouse ovaries [65] and zebrafish embryos [66]. Next, samples were loaded onto a microscope stage and images of motile spermatozoa were acquired from ex vivo cauda epididymis (Fig. 2A).

The autofluorescence of NAD(P)H allowed us to visualize living motile spermatozoa within cauda epididymis (Fig. 2A). Similar to immobilized sperm (Fig. 1A), the fluorescence intensity of NAD(P)H in the midpiece was brighter than in the heads and flagellar principal pieces both of which exhibited weaker NAD(P)H fluorescence intensity (Fig. 2A). In contrast to immobilized sperm, the lifetime of NAD(P)H in motile sperm was shorter in the head and principal piece compartments, but longer in mitochondria (Fig. 2B, C). Such compartmentalization of NAD(P)H in motile spermatozoa aligns with previous studies suggesting that glycolysis associated with higher fraction of the free NAD(P)H prevails both in the principal piece and the sperm head, and OXPHOS, indicated by higher fraction of bound NAD(P)H, occurs in the mitochondrial midpiece [60–62].

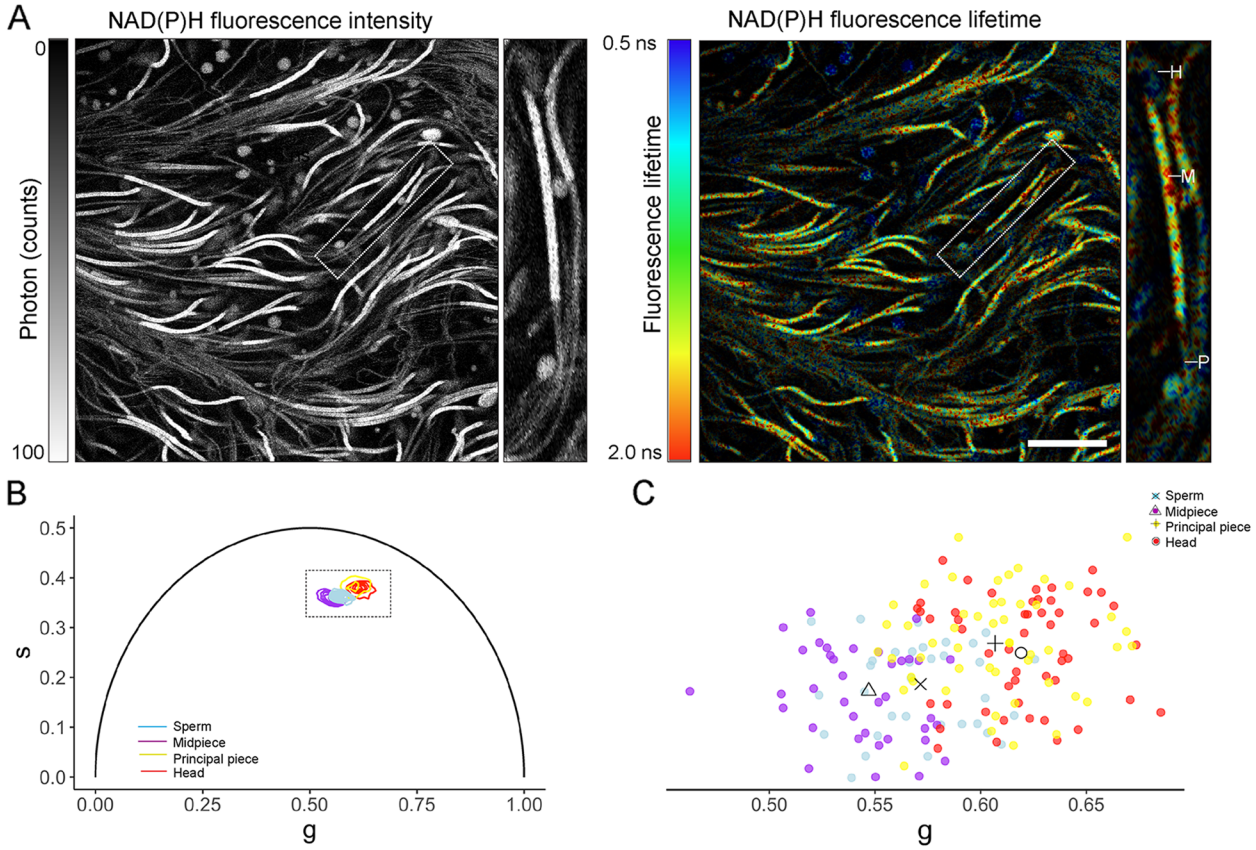

Fig. 2 In situ 2P-FLIM NAD(P)H imaging unveils the native metabolic state of motile spermatozoa. **A** Greyscale image of NAD(P)H fluorescence intensity signals (left) and color-coded image of NAD(P)H fluorescence lifetimes (right). Note the increased cellular autofluorescence in the mitochondria-rich midpiece in both images, as well as in the zoom insets displaying the spermatozoon. **B** Object-based phasor plot and **C** the individual points display the metabolic states of motile spermatozoa and subcellular compartments including the midpiece, head, and principal piece. H, head; M, midpiece; P, principal piece. Scale bar, 20 µm

We next imaged FAD within motile spermatozoa in situ using 2P-FLIM. As expected, the intensity and lifetime of FAD was restricted to the midpiece, whereas the head and principal pieces were dim (Additional file 3: Fig. S3). In contrast to immobilized sperm, FAD imaging in motile sperm accurately reflects its role in mitochondrial metabolism. Although NAD(P)H and FAD are often used together for metabolic imaging [32], sperm movement during imaging prevented simultaneous acquisition of NAD(P)H and FAD for the same motile spermatozoa using dual wavelength excitation. Although it is possible to image simultaneously NAD(P)H and FAD with single wavelength excitation [67], this approach requires specialized emission filters and leads to lower signal-to-noise ratio due to suboptimal excitation wavelength for both cofactors. We therefore focused on NAD(P)H imaging for quantitative analysis for two reasons. First, NAD(P)H lifetimes provide quantitative measurements of each metabolic compartment in individual spermatozoa, whereas FAD only yields quantitative readouts of sperm mitochondrial metabolism. Second, because NAD(P)H levels were higher than FAD, lower excitation power was needed for imaging, which helped maintain sample viability.

To compare the metabolic states in immobilized and motile sperm, we segmented manually individual sperm and subcellular compartments from FLIM images and conducted object-based phasor analysis. The resulting phasor plots distinguished the metabolic states between motile and immobilized sperm (Additional file 4: Fig. S4). The mean g phasor values for mitochondrial midpiece (probability counted using linear model (lm) $P = 0.003$), head ($P = 0.045, \mathrm{lm}$) and principal piece ($P = 0.032, \mathrm{lm}$) compartments differed between motile and immobilized states, as well as for single spermatozoa ($P = 0.037, \mathrm{lm}$). This comparative analysis confirmed that immobilizing sperm with coverslips significantly alters their metabolic profile. Our findings raise concerns on the reliability of metabolic imaging data obtained from immobilized sperm, which may not faithfully capture all the

metabolic features. By introducing a new sample preparation method that involves hydrogel encapsulation of cauda epididymis we avoid sperm immobilization prior to imaging. NAD(P)H and FAD lifetimes can be thus imaged in motile sperm. In sum, we directly visualize for the first time that NAD(P)H is compartmentalized in motile mouse spermatozoa, with levels that vary in subcellular domains and exist in both free and protein-bound form—as previously observed for oocytes [65], embryos [68], somatic cells [52, 69], and stem cells [70].

Automated segmentation of sperm compartments from FLIM images using deep learning

The quantitative analysis of FLIM images requires segmentation of individual sperm cells and subcellular compartments in order to extract object-based lifetime information. Since manual segmentation is both labor and time-consuming, we implemented a machine-learning algorithm based on U-Net [71] for automated segmentation of sperm structures from FLIM images. First, FLIM images were manually annotated (see Methods); segmentation of bright and clearly delineated structures such as mitochondria in the midpiece was straightforward (Fig. 3A). Subcellular structures displaying reduced fluorescence intensity, i.e., sperm heads and principal pieces, proved more challenging. Adjusting the brightness of FLIM images allowed us to identify sperm head boundaries and facilitated segmentation (Fig. 3C). Sperm motility induced sample motion during image acquisition and rendered principal pieces in proximity and thus difficult to discriminate unambiguously. For this reason, we did not automatically segment principal pieces from FLIM images. By making our data available, we anticipate that future work will aid in their segmentation.

To assess the quality of the segmentation, we compared the performance of our U-Net to manually labeled ground truth using a test set of FLIM sperm images, which were used neither for training nor for validation. In comparison to the ground truth, our model achieved an accuracy of 92.8 ± 0.09, recall 71.2 ± 0.59, precision 80.90 ± 0.66 and F1-score 75.7 ± 0.34 for both midpiece and head segmentation. Next, we carried downstream analysis of the resulting segmented images for further testing of our U-Net (Fig. 3B, C) using phasor analysis as above [58]. Object-based phasor coordinates, g (x) and s (y) derived from the FLIM data were then plotted to generate fingerprints for all segmented objects (Fig. 3B, C). We found that phasor fingerprints of automatically segmented midpieces and heads overlapped well with the ground truth. The g coordinate values were comparable and statistically insignificant between automated and manually segmented midpieces ($P = 0.97$, Wilcoxon test) and sperm heads ($P = 0.202$, lm). Thus, our automated model is well trained and on par with manual segmentation.

Sperm and midpiece NAD(P)H metabolic fingerprints distinguish mouse strains from two subspecies

Once we established 2P-FLIM acquisition, FLIM image segmentation and object-based phasor analysis of sperm

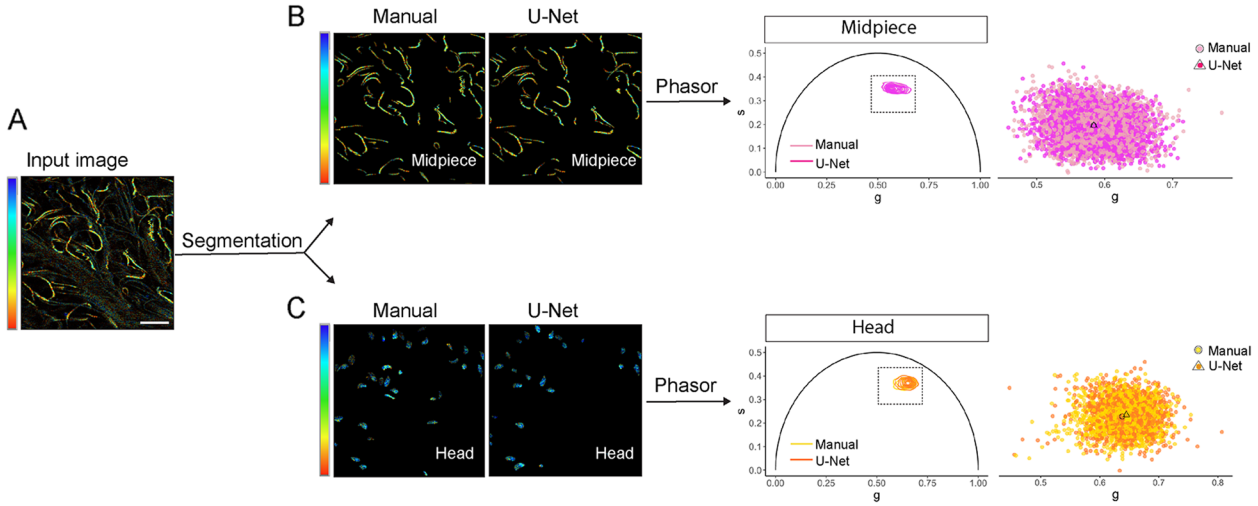

Fig. 3 U-Net segmentation is on par with manual segmentation. **A** An input FLIM image is used to segment: **B** midpiece and **C** head structures. Segmentation was performed manually and automatically by U-Net, respectively. Object-based phasor fingerprints were generated to compare the performance of U-Net to manual segmentation. In total, 2123 manual and 2437 U-Net segmented midpieces were compared. In the case of sperm heads, 1136 manual and 1037 U-Net generated objects were compared. As shown in phasor graphs, fingerprints of midpiece, and head objects overlapped well for both manual and U-Net segmentation. Means (empty triangles and circles) are plotted in the graphs along the data points of individual cells or objects (dots). Scale bar, 20 µm

NAD(P)H lifetimes, we then tested the performance of this workflow for metabolic fingerprinting of spermatozoa through several experiments. In *Mus* species, spermatozoa are metabolically heterogeneous [72, 73]. Males that produce more metabolically active, and thus faster sperm are more likely to fertilize the egg [74]. Metabolic heterogeneity in sperm is thus physiologically important, but whether differences in sperm metabolism are exclusive to the *Mus* species or represent the norm remains unclear. *M. m.* subspecies vary in sperm traits, i.e., count, size, and motility [75], but metabolic differences have not been documented. To fill this gap, we generated sperm metabolic profiles of wild-type mouse subspecies using our workflow (Additional file 2: Fig. S2). For this first set of experiments, we imaged NAD(P)H within sperm of three strains from two closely related house mouse subspecies: PWD/Ph (henceforth PWD, *M. m. musculus*), C3H/N (C3H) and C57BL/6J (B6; both *M. m. domesticus*) (Fig. 4A). As expected, the autofluorescence signal was derived mostly from mitochondria in the midpiece region, while a weaker NAD(P)H signal was observed in the head and principal piece compartments of all strains (Additional file 5: Fig. S5A). We then generated single-cell (by manual segmentation) and subcellular (midpiece and head automatically; principal piece manually) phasor fingerprints (Figs. 4B, C, Additional file 5: S5B, C). We observed metabolic clusters specific to each of the three mouse strains on plots depicting sperm and midpiece fingerprints (Fig. 4B, C). The mean phasor *g* values of spermatozoa differed significantly between PWD and B6 mice ($P_{adj.}$= 0.006, lm, Tukey's method), but not between PWD versus C3H, and C3H vs. B6 (both $P_{adj.} \geq 0.05$). Midpiece phasor *g* values differed for all mouse strains including PWD vs. C3H ($P_{adj.} = 0.034$), PWD vs. B6 ($P_{adj.} < 0.001$) and B6 vs. C3H ($P_{adj.}$= 0.001) (Fig. 4B, C). When sperm head *g* values were compared, there were no differences between the strains (all $P_{adj.} \geq 0.05$, Additional file 5: Fig. S5B, C). The same was true for principal piece fingerprints (all $P_{adj.} \geq 0.1$). Therefore, mitochondrial OXPHOS, but not glycolysis, was the main source of heterogeneity in sperm metabolic signatures among these three strains.

Single-sperm and midpiece metabolic profiles correlate with male fertility

In vertebrates, males with faster-swimming spermatozoa achieve higher fertilization rates [76] and sire more offspring [77]. As faster spermatozoa require more ATP, selection should in theory favor adaptations that result in higher sperm energy metabolism. Indeed, in both non-mammalian and mammalian vertebrates the sperm midpiece is under strong selection and evolves rapidly compared to the principal piece [78]. This may explain why we observe heterogeneity in OXPHOS, but not glycolysis in mouse strains. Based on this, we hypothesized that males with higher sperm metabolism, specifically OXPHOS, might be more fertile. This does not imply that glycolysis in the principal piece is irrelevant for male fertility, but rather that we focused on mitochondrial OXPHOS as it evolves rapidly, was heterogeneous in males, and yields more ATP.

Sperm motility, morphology, and count are used as surrogate markers of male fertility. Studies suggest that these parameters are not sufficient; hence, the average litter size sired by males needs to be taken into account, for example, when testing the effects of new drugs on male fecundity [79]. For this reason, we used the offspring number (litter size) sired by males as a more reliable marker of male fertility. We then addressed the question of whether potential correlations exist between the mean sperm metabolic profiles and the mean litter size (Fig. 4D). Notably, there was a strong inverse correlation between sperm phasor *g* values (Pearson's correlation $r = -0.71$, P=0.01) and the litter size, suggesting that spermatozoa with lower *g* values (and increased bound NAD(P)H) had higher fertilizing ability. A similar correlation was obtained between midpiece *g* values and the litter size (Fig. 4D), indicating that increased bound NAD(P)H, and thus higher mitochondrial activity, might be advantageous for male fertility. Our data suggests that sperm NAD(P)H metabolism may influence fertilization success, which could be used for selecting sperm to potentially increase in vitro fertilization rates. Given that sperm selection in the female reproductive tract is a multistep process [80, 81], it is unlikely that a single marker can accurately predict fertilization success. Traditional markers such as sperm count, morphology, and motility often fall short in predicting fertilization success, as evidenced by in vitro fertilization failures despite sperm selection based on these markers [80, 81]. A combined approach using several markers, including metabolic fingerprints, may predict more accurately the fertilization ability of sperm. Future studies should investigate how sperm metabolism influences fertilization success, either directly or by boosting sperm swimming speed.

Sperm metabolic fingerprints can differentiate fertile and subfertile mice

The observed correlation between male fertility and the OXPHOS compartment (Fig. 4D) predicts that sperm with decreased mitochondrial activity, motility (asthenospermia) and fertility would exhibit different metabolic signatures compared to normal motile sperm. To test this hypothesis, we compared metabolic fingerprints of normospermic fertile and asthenospermic subfertile mice. For this feasibility study, we used F1 male offspring

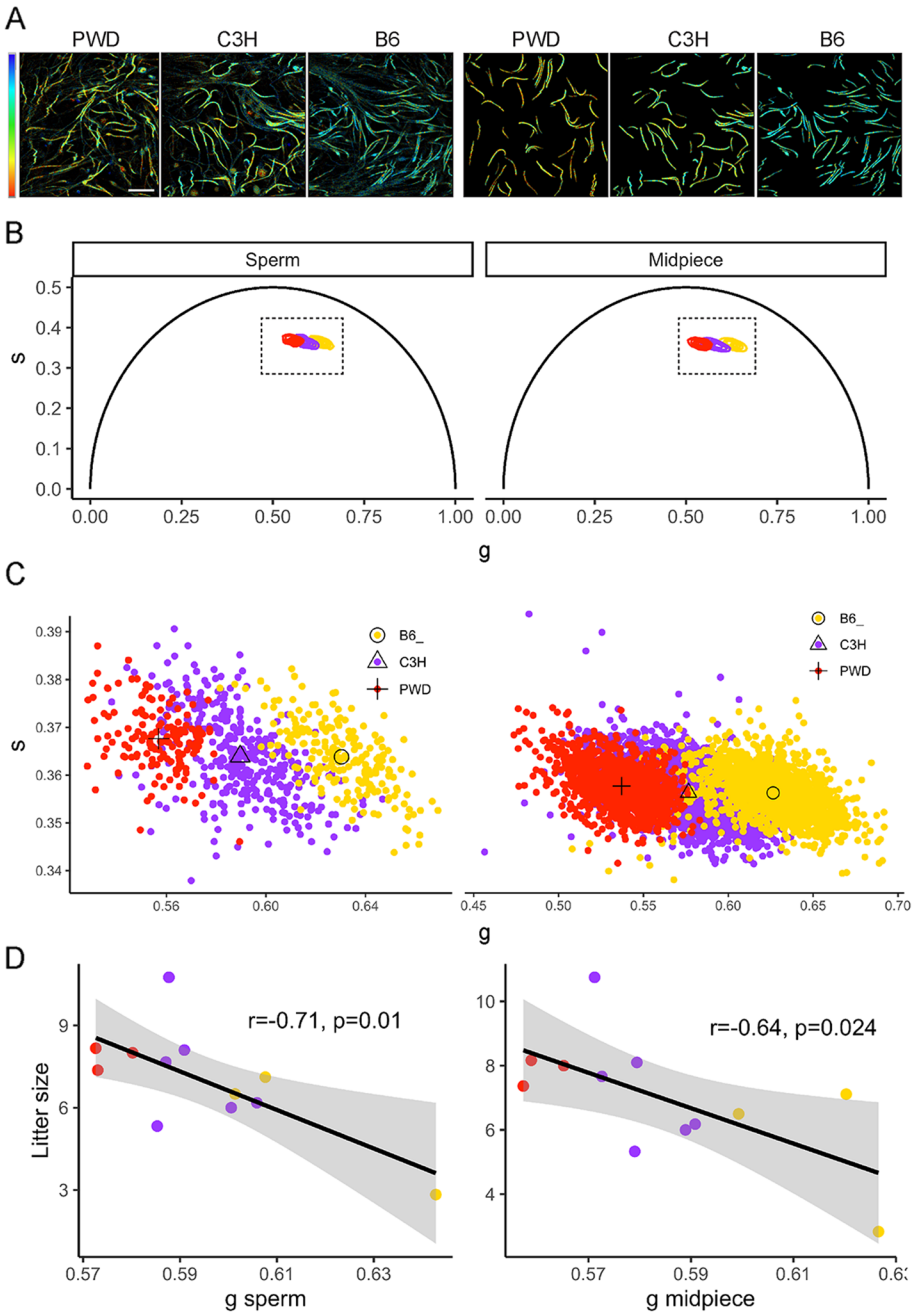

Fig. 4 Object-based phasor metabolic fingerprints distinguish sperm midpieces of three mouse strains. **A** Representative FLIM images of PWD (*M. m. musculus*), B6 and C3H (*M. m. domesticus*) depicting whole sperm cells and U-Net-segmented midpiece subcellular compartments, respectively. Metabolic fingerprints in **B** and **C** are different for each strain at the single-cell and subcellular midpiece levels. Sperm phasor fingerprints of PWD (2 males, 149 cells), B6 (3 males, 207 cells), and C3H (6 males, 632 cells) were generated manually. U-Net segmented midpieces of PWD (2 males, 1426 objects), B6 (3 males, 1646 objects), and C3H (6 males, 3208 objects) strains. **D** Phasor *g* values of sperm and midpiece fingerprints correlated significantly with male's reproductive success given as litter size. Every filled circle represents the mean value for one male, color-coded by strain as the single sperm cell and midpiece values above

from crosses between B6 females and PWD males as a subfertile mouse model. Unlike their PWD fathers, (B6 × PWD)F1 hybrids (hereafter, B6PF1) are asthenospermic and this coincides with decreased mitochondrial activity due to malformations in the mitochondrial sheath [82]. Using FLIM, we imaged NAD(P)H of spermatozoa in situ (Figs. 5A & Additional file 6: Fig. S6A). After manual cell segmentation, single sperm fingerprints were generated

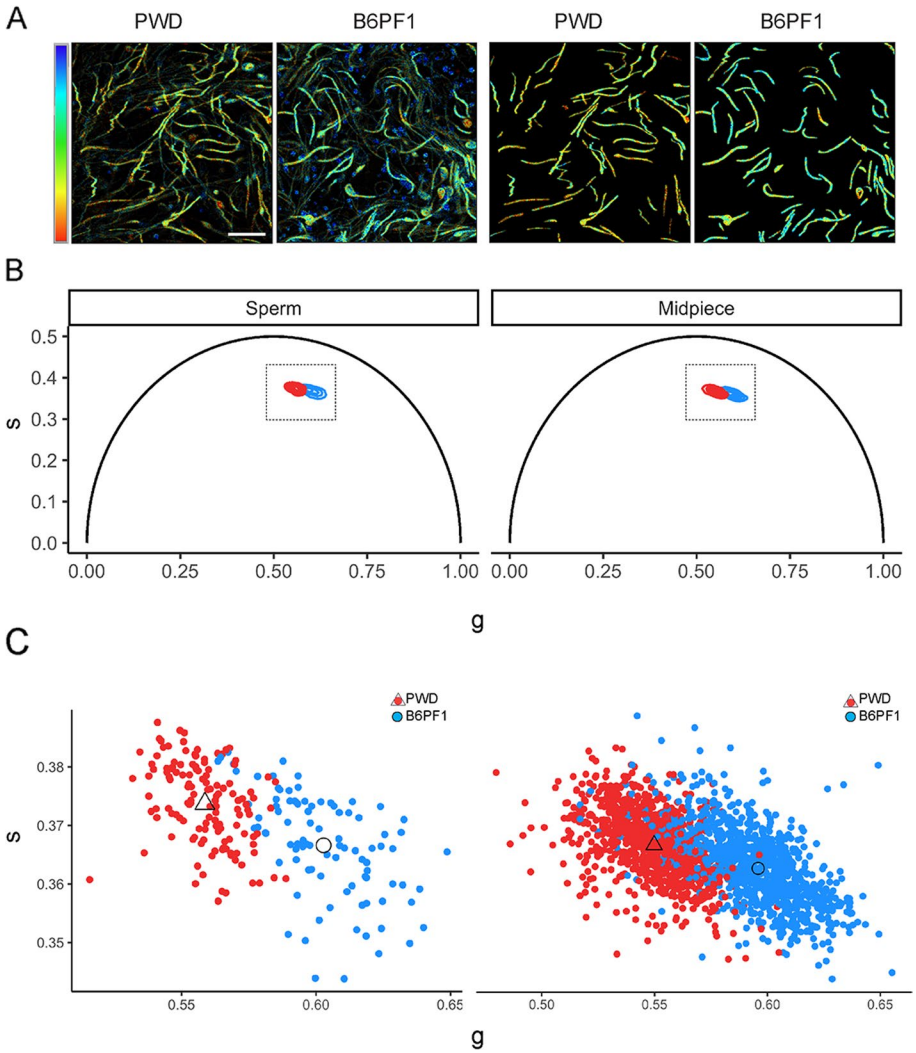

Fig. 5 Metabolic fingerprints of spermatozoa and midpieces differed between fertile and subfertile males. **A** Representative FLIM images of sperm cells and midpiece mitochondrial compartments. Object-based phasor fingerprints **B** and **C** show two distinct clusters corresponding to PWD (fertile) and B6PF1 (subfertile) males. Sperm phasor fingerprints of PWD (4 males, 107 cells) and B6PF1 (2 males, 91 cells) were generated manually. U-Net segmented midpieces of PWD (4 males, 1016 objects) and B6PF1 (2 males, 957 objects) automatically. See Additional file 6: Fig. S6 for head and principal piece fingerprints. Scale bar, 20 µm

using phasor analysis (Fig. 5B, C). We observed two separate clusters of individual sperm values on the phasor plot, indicating distinct metabolic profiles of B6PF1 and PWD sperm cells. The *g* coordinate values of single sperm differed between B6PF1 and PWD mice ($P = 0.045$, generalized least squares [gls]). To investigate whether these differential cellular metabolic signatures reflect differences in mitochondrial metabolism, we used our automated network to segment mitochondria and generated phasor fingerprints. Sperm mitochondria of B6PF1 subfertile mice were separated in the phasor plot and showed a different metabolic state ($P = 0.002$, lm) compared to PWD fertile controls (Fig. 5B, C). There were no significant differences in the head and principal piece metabolic profiles between these two mouse genotypes (Additional file 6: Fig. S6B, C).

We previously reported that B6PF1 had ~ 63% increase in midpiece malformations compared to PWD controls [82], likely contributing to the observed differences in OXPHOS metabolism. However, not all B6PF1 sperm are malformed. Some exhibit normal morphology, motility [82], and can fertilize eggs in vivo [83], suggesting phenotypic similarities with PWD. To test this in the context of metabolism, we calculated the overlap in *g* values between the PWD and B6PF1 midpieces by setting a threshold based on each group's mean and

standard deviation. Indeed, 41.5% of *g* values overlapped (Additional file 7: Fig. S7), suggesting that around 40% of B6PF1 spermatozoa share similar OXPHOS profiles with PWD controls, while the rest (~60%) differ. Although the overlap percentage changes depending on threshold, this analysis suggested metabolic similarities between some B6PF1 and PWD sperm. Overall, our method based on NAD(P)H autofluorescence lifetime effectively captures both metabolic differences and similarities, likely reflecting the metabolic quality of sperm.

Young and old males differ in metabolic fingerprints of spermatozoa

While mitochondria produce ATP and maintain energy homeostasis, they also generate reactive oxygen species (ROS) as a by-product of normal aerobic metabolism. Increased mitochondrial ROS production, e.g., during aging, causes oxidative damage to nucleic acids, lipids, and proteins [84]. Mitochondrial dysfunction and oxidative stress are thus implicated in aging of soma [85] and gametes [86]. Spermatozoa are more susceptible to oxidative damage than somatic cells, which upregulate antioxidant gene expression to counteract ROS [87]. Mature spermatozoa have compacted chromatin and thus lack transcription and DNA repair proteins, which render them defenseless against ROS. Moreover, spermatozoa's high demand for ATP results in exposure to ROS over time, inflicting DNA damage that is likely to accumulate without repair [88, 89]. Indeed, studies report of oxidative damage in aged mouse [90, 91] and human sperm [92, 93], as well as mitochondrial metabolite changes in turkey sperm with aging [94]. Motivated by these studies, we investigated the impact of aging on the mouse sperm metabolism using our FLIM workflow. We generated sperm metabolic signatures in young adult (~4 months) and old (~18 months) PWD mice. We observed a shift of single spermatozoa in the phasor plot with age (Fig. 6A, B), closer to the bound NAD(P)H (that is, oxidative metabolism). This shift and decrease in the mean *g* value of old mouse spermatozoa when compared to the young ones ($P = 0.024$, lm) was at the expense of the midpiece ($P = 0.032$, lm) and head ($P = 0.0167$, lm) compartments (Figs. 6A and Additional file 8: Fig. S8A). However, this was not accompanied by any changes in the principal piece ($P = 0.41$) (Additional file 8: Fig. S8A, B), suggesting that glycolysis was unaffected by age. If it holds true that old mouse spermatozoa have increased oxidative stress compared to younger ones, we should be able to recapitulate age-related metabolic profiles by exposing sperm to increased ROS levels, e.g., by adding H_2O_2. As expected, treatment with H_2O_2 shifted young sperm into a state of oxidative stress, such that their phasor position was closer to the bound NAD(P)H concomitant with a significant decrease in the *g* value when compared to control sperm ($P = 0.02$, gls) (Fig. 6C, D). There were no changes detected in the head ($P = 0.686$, gls) and principal piece ($P = 0.324$, gls) (Additional file 8: Fig. S8A, B), implying that midpiece mitochondrial changes ($P = 0.0147$, gls) account for the observed oxidative shift (Fig. 6C, D).

Glycolysis inhibition increases oxidative damage in ram sperm [95], presumably by enhancing OXPHOS and mitochondrial ROS generation. Based on this observation, we tested whether glycolysis inhibitors, such as 2-DG, increase oxidative stress in mouse spermatozoa. Similar to H_2O_2 treatment, 2-DG significantly decreased the mean *g* value of sperm metabolism ($P = 0.005$, lm) including mitochondria ($P = 0.001$, lm), as a result of increased bound NAD(P)H and OXPHOS (Additional file 9: Fig. S9). Thus, the acute exposure to oxidative stress generated by H_2O_2 or 2-DG shifted the mouse sperm metabolism to an aging-like phenotype.

Conclusions

By combining hydrogel encapsulation of cauda epididymis, 2P-FLIM, automated image segmentation, and object-based phasor analysis, we developed a new tool for label-free NAD(P)H imaging of living motile spermatozoa with subcellular resolution. Our approach offers several advantages over current state-of-the-art metabolic assays. First, our sample preparation avoids the need for metabolite extraction, which is both slow and invasive. Second, we use label-free contrast to capture metabolic information, and thus bypass the limitations that come with fluorescent dyes, i.e., specificity, impermeability, and toxicity. This is particularly important for clinical application, where fluorescent labeling of spermatozoa is not allowed. Third, we eased the burden of image segmentation by training U-Net to segment sperm metabolic compartments. Our trained U-Net segmented automatically 17,326 midpieces and 8930 heads. This approach is computationally fast, performs hours of human work in minutes, and increases throughput for statistics. Fourth, quantitation of metabolite(s) lifetime within individual sperm cells and subcellular compartments can unveil metabolic heterogeneity in sperm populations of physiological and pathological states, such as infertility. Our approach could be further developed into a method that allows for selection of spermatozoa for assisted reproduction based on metabolic parameters. For clinical translation, future work should test high-speed FLIM technologies for NAD(P)H imaging in freely moving sperm. Since the flagellum of human spermatozoa beats around 20 times/s [96], laser multiplexing [97] combined with 2P-FLIM acquisition at 25 fps [43] could

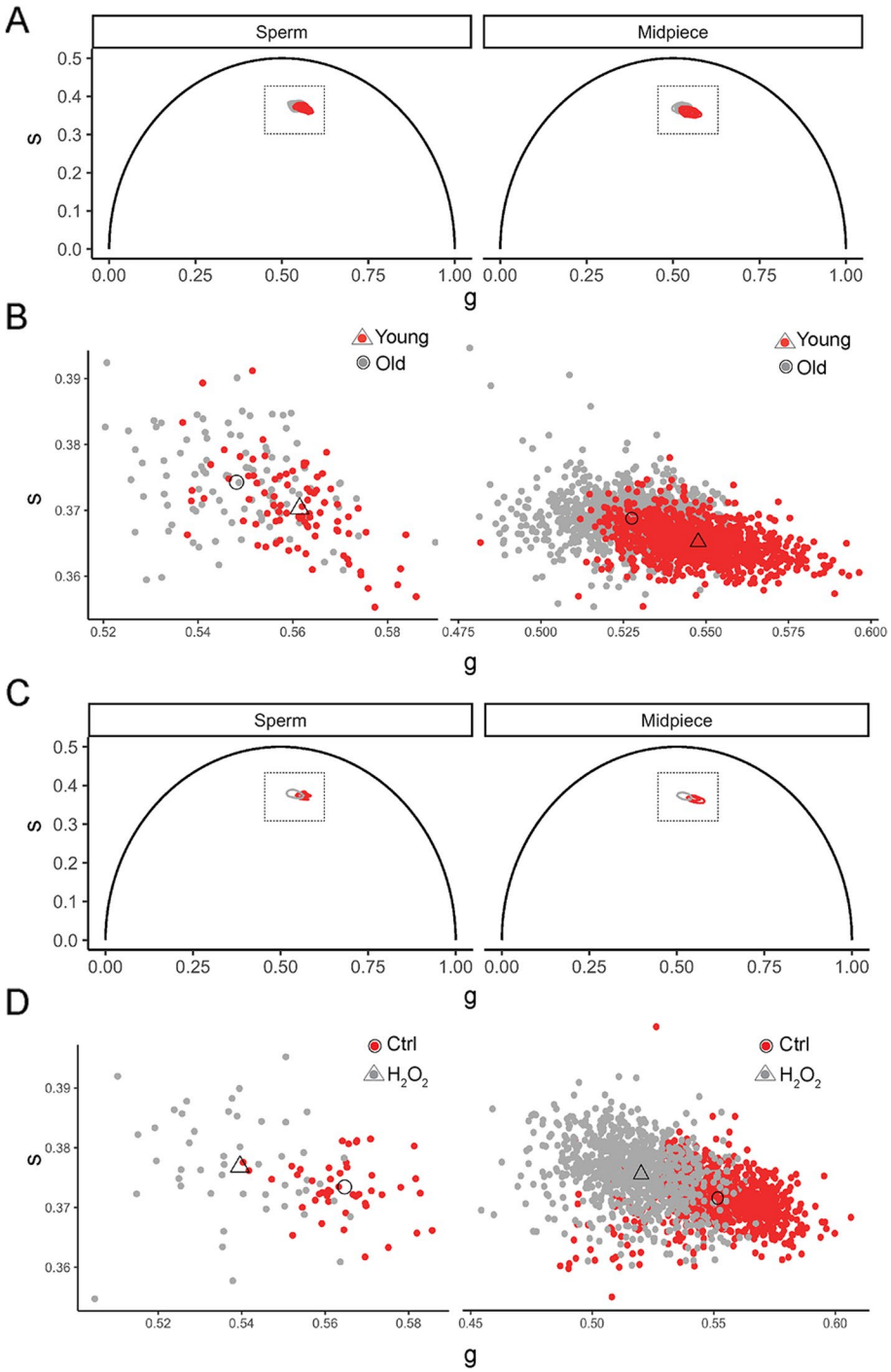

Fig. 6 Sperm and midpiece object-based phasor fingerprints detected an increase in OXPHOS metabolism with age. Phasor fingerprints **A** and **B** of PWD spermatozoa from old males are shifted toward bound NAD(P)H when compared to young males. Sperm cells from old (3 males, 102 cells) and young (3 males, 45 cells) males were generated manually. Midpieces from old (3 males, 1040 objects) and young (3 males, 1003 objects) mice were segmented using U-Net automatically. See Additional file 8: Fig. S8 for head and principal piece metabolic fingerprints. Object-based phasor plots in **C** and **D** depict spermatozoa treated with 50 µM H_2O_2 and untreated controls. Sperm cells from H_2O_2-treated (2 males, 46 cells) and control (2 males, 43 cells) males were generated manually. Midpieces from H_2O_2-treated (2 males, 945 objects) and control (2 males, 949 objects) sperm were segmented using U-Net automatically. Treatment of sperm from young males with H_2O_2 resulted in a phasor shift toward bound NAD(P)H, indicating increased OXPHOS metabolism. The treatment of sperm with 2-DG also induced an increase in OXPHOS activity (Additional file 9: Fig. S9)

potentially capture the metabolism of human sperm in suspension. Alternatively, spermatozoa could be encapsulated in a biosynthetic gel that mimics the shape of cauda epididymis to resemble our approach.

Methods

Mouse work

Animal experiments complied with the Czech Republic Act for Experimental Work with Animals (Decree 419/2012, Laws 246/1992 and 501/2020) and Europian Union Council Directives including 2010/63/EU.

The wild-derived PWD/Ph mouse strain of *M. m. musculus* lineage was described in [98]; the C57BL/6J (B6) strain of *M. m. domesticus* lineage was purchased from The Jackson Laboratory (Stock no. 000664) and C3H/N (*M. m. domesticus*) from Velaz, Czech Republic. All strains were inbred and housed in the Animal Facility of the Institute of Molecular Genetics in Prague. Mice were euthanized by cervical dislocation followed by diaphragm incision.

In vivo fertility assay

In vitro fertilization bypasses the natural barriers of sperm selection that take place inside the female reproductive tract [80, 81]. To avoid this, we tested male fertility under in vivo conditions. Fertility of wild-type male mice of different strains including PWD, B6, and C3H was tested in three mating experiments (2–5 males/strain/experiment). Each male (10–30 weeks old) was caged with two wild-type females (10–30 weeks old) of the same strain where possible; otherwise, B6 females were used. As soon as the dams had delivered, the number of pups was counted to exclude the effect of preweaning loss. The average litter size was calculated by dividing the number of pups recorded for each litter by the number of litters produced. The average litter size calculated from three independent experiments per male/ strain was used for correlation analysis.

Sperm immobilization prior to imaging

Spermatozoa from PWD males were isolated from cauda epididymides in a 35-mm Petri dish containing 2 ml of Hank's balanced salt solution (HBSS, recipe below) heated to 37°C. Aliquots of spermatozoa (~10,000 cells) were pippetted onto coverslips (18 mm diameter) coated with 1% low melting point agarose (LMPA, Promega) in HBSS. An additional (uncoated) coverslip was added on top. This method of sandwiching spermatozoa between LMPA-coated coverslip (at the bottom) and uncoated coverslip (at the top) minimized the movement of spermatozoa and allowed imaging using the set-up described below.

Hydrogel sample preparation

Epididymides were dissected and placed in a 35-mm Petri dish containing 2 ml HBSS (136 mM NaCl, 5 mM KCl, 1 mM $CaCl_2$, 0.4 mM $MgSO_4 \times 7H_2O$, 0.5 mM $MgCl_2 \times 6H_2O$, 0.2 mM $Na_2HPO_4 \times 2H_2O$, 0.5 mM KH_2PO_4, 5.5 mM glucose, and 4 mM $NaHCO_3$ pH 7.4) heated to 37°C. Under a stereomicroscope, cauda epididymis was then cut in the HBSS medium (as shown in Fig. S2) and placed in a 35-mm one-well magnetic chamber (Chamlide CMB, Live Cell Instrument) having an 18-mm-diameter round coverslip at the bottom. The chamber was filled with 1 ml 1% LMPA (Promega) in HBSS and mounted in a stage top incubator (OKOlab) at 37°C with 5% CO_2.

Hydrogen peroxide (H_2O_2) and 2-deoxyglucose (2-DG) treatments

After isolating epididymides as detailed above, paired cauda epididymides from each male were split into control and treated groups. The control group consisted of cauda placed into the Chamlide chamber filled with 1% LMPA in HBSS. The treated group was incubated with H_2O_2 (Sigma) to a final concentration of 50 µm (diluted and mixed with 1% LMPA in HBSS) into the Chamlide chamber for 10 min prior to imaging. For 2-DG treatment, cauda epididymides were treated with 10 mM 2-DG (Sigma) in 1% LMPA in glucose-free HBSS for 1 h and imaged. For both control and 2-DG treated groups, glucose-free HBSS was supplemented with 20 mM sodium lactate (Sigma) and 1 mM sodium pyruvate (Sigma). Control and treated groups were enclosed in a heated incubator (OKOlab) maintained at 37°C with 5% CO_2 flow for all FLIM experiments, as described below.

Two-photon fluorescence lifetime imaging microscopy (2P-FLIM) setup

2P-FLIM of caudal spermatozoa was performed on a Carl Zeiss LSM 880 NLO inverted scanning confocal microscope controlled with Zen Black 2.1 software. Two-photon excitation was supplied by a Titanium:Sapphire femtosecond laser Chameleon Ultra II (Coherent) pulsing at 80 MHz, optimized by pre-chirp (femtoControl, APE Angewandte Physik & Elektronik GmbH) resulting in 200 fs pulse width at the sample. In 2P-FLIM, fluorophores are excited with two photons simultaneously: each photon has approximately twice the wavelength and half the energy of the one photon required for one-photon excitation. For this reason, endogenous fluorophores NADH and NADPH were excited at 740 nm and

FAD at 900 nm using a Carl Zeiss C-Apochromat 40×/1.1 W Corr objective. The laser power applied to the sample was ≤ 13 mW. A short pass dichroic mirror (690 nm) was used to separate the fluorescence signal from the laser light and a short pass filter (485 nm for NADH and NADPH; 500 nm for FAD) was placed in front of hybrid detector, HPM-100–40 (Becker & Hickl), placed at non-descanned port, attached to a time-correlated single photon counting electronics HydraHarp 400 (PicoQuant). Prior to imaging samples, we first calibrated the FLIM system using 0.5 μM Coumarin-6 (Sigma) solution in 100% ethanol with a reference lifetime of 2.5 ns [99]. To obtain high signal-to-noise ratio, we acquired typically 16 frames of 512 × 512 pixels for each field of view. The acquisition time was 83 s (5.19 s per frame) at a speed of 5 μs/pixel with 2×zoom in monodirectional scanning mode. FLIM data were recorded using the SymPhoTime 64 software (PicoQuant).

Preparation of free and bound NADH solution

NADH (Sigma) solution was prepared in 100 mM morpholino propanesulfonic acid (MOPS, pH 7) at a final concentration of 250 μM NADH was then mixed in 1:1 ratio with 1000 unit/ml lactate dehydrogenase (LDH, Sigma) as described [46]. Both free NADH and NADH-LDH (bound) solutions were measured at 740 nm using the 2P-FLIM imaging set-up as described above.

U-Net segmentation network architecture

U-Net is a state-of-the-art convolutional neural network developed for fast and precise biomedical image segmentation [71]. U-Net-based networks are easy to implement and can achieve accurate image segmentation from training with only 30–50 microscopy images [100]. We thus adapted U-Net [71] to segment sperm structures from our FLIM dataset and slightly modified its original architecture. The U-Net's general architecture consists of two parts, an encoder downward part and a decoder upward path [71]. The encoder path of our U-Net variant is composed of five down-sampling blocks. Each block has the following structure: first, to extract and encode spatial features we used a convolution layer of kernel size 3 × 3 with stride 1 (as in all convolutional layers, unless specified otherwise) and a rectified linear unit activation function (ReLU) followed by a batch normalization layer. A convolution layer with a kernel size 2 × 2 with stride 2 is applied at the end of each down-sampling block to halve the spatial resolution and double the number of feature channels. In the decoder path, there are five corresponding up-sampling blocks, each of which consists of 2 × 2 transposed convolutional layers with stride 2 and ReLU to double the spatial resolution of the output (that is, image pixels) and halve the number of feature channels. To prevent loss of information in the decoder path, we used a skip connection to concatenate the feature maps from the encoder path with the corresponding layer in the decoder path. After each skip connection in the upsampling block, three convolutions with kernel size 3 × 3 and ReLU are applied, each followed by batch normalization. The final 1 × 1 convolutional layer uses soft-max activation to generate probability masks. The encoder and decoder pathways are connected by 3 ×3 convolutional layers with ReLU, which lie at the bottom of the U-shape network architecture. All convolutional layers use the same padding to keep the spatial dimensions unchanged in the final segmentation masks.

FLIM dataset preparation and U-Net model training

We generated manual annotations of sperm structures from FLIM images with the goal of developing a U-Net-based segmentation model. To create the dataset, we used FLIM images of three mouse strains and their hybrids: PWD, C3H, B6, (C3H × PWD)F1, and B6PF1 males to represent the variability in terms of sperm density, morphology, and flagellar movement. FLIM images of different mouse strains were chosen from several independent males and experiments to eliminate biases. In total, 21,907 midpiece and 10,465 head structures of spermatozoa were manually labeled using the NIS Elements binary editor tool (Nikon). Overall, midpieces were easy to distinguish and their labeling was straightforward. However, sperm heads proved more challenging because of the weaker intensity and hook-shaped morphology. In some cases, sperm heads had very weak intensity and it was difficult to label them even when adjusting the brightness of FLIM images. In other cases, sperm heads were out of frame or too close for them to be distinguished unambiguously between two spermatozoa. All these factors contributed to our dataset having more midpiece labels compared to heads. In total, the labeled dataset consisted of 281 FLIM images of 512 × 512 pixels with corresponding binary masks of midpieces and heads. The set of original images and the manually annotated masks were used for training, validation, and testing of our U-Net variant. In general, to develop U-Net-based models most of the annotated dataset is used for training (80%) and a smaller set for validation and testing (10–20%) [100–104]. We followed a similar strategy and used for training 235 FLIM images with a total of 17,952 midpieces and 8620 heads labeled. The validation set consisted of 16 images with 1488 midpieces and 678 heads labeled. Whereas the test set had 30 images with 2507 midpieces and 1167 heads labeled. To reduce the number of animals used for the experiments, we applied several data augmentation techniques to artificially increase the size of the training set (only

during training). Augmentation was performed utilizing rotations of all degrees in combination with vertical flip with probability 50% and cropping to a resolution of 256 × 256 pixels at random locations. We trained our network with a batch size of 32 images per iteration using the Adam algorithm [105] with the initial learning rate set to 5×10^{-4}. We applied a learning rate decay by a multiplying factor of 0.5 every 20 epochs. The weighted pixel-wise cross-entropy was used as the loss function. To compensate for class imbalances in our dataset, we gave static weights to each class: background (weight = 2), midpiece (weight = 2), and head (weight = 3). Weights of all convolutional layers were initialized according to He normal distribution [106], and each convolutional layer was regularized with L2-regularization with a factor of 0.001. The model was evaluated on the validation set every 10 epochs during training and the model with the highest overall F1-score in the validation set was saved. Our network training was implemented in Python using Tensorflow [107] and Keras libraries. On average, training took ~ 2 h on a single Quadro RTX 500 16 GB GPU.

The performance evaluation of our U-Net model

We trained the model as described above and selected the best model according to the validation set. The final performance of the trained model was evaluated using the test set of FLIM images ensuring that the same images were not used for training or validation. To compare the segmentation masks from our model and ground truth masks (that is, manually annotated), we first needed to match midpieces and heads of the automated model and manual masks. Matching was done using the Hungarian algorithm [108], which minimizes the distance between individual mask objects. This distance (d) is calculated Intersection-over-Union (IoU) for each pair of masks, m_i from the manual and m_j from the automated network segmentation using the equation detailed below and described in [109, 110]:

$$\mathrm{IoU}(m_i^{man}, m_j^{net}) = \frac{\left| m_i^{man} \cap m_j^{net} \right|}{\left| m_i^{man} \cup m_j^{net} \right|} \tag{1}$$

where the d is defined as:

$$d\left(m_i^{man}, m_j^{net}\right) = \begin{cases} 1 - \mathrm{IoU}(m_i^{man}, m_j^{net}), & \mathrm{IoU}(m_i^{man}, m_j^{net}) \geq 0.4 \\ 0, & m_i^{man} \subseteq m_j^{net} \text{ or } m_j^{net} \subseteq m_i^{man} \\ \infty, & \text{otherwise} \end{cases} \tag{2}$$

We calculated IoU for every pair of manual and automated segmented masks and applied the Hungarian algorithm using the distance matrix (Eq. **2**) to obtain true positive (matched) or unmatched masks. In Eq. **2**, d=∞ denotes masks that cannot be matched due to their small IoU score. We then calculated four metrics including pixel-wise accuracy, recall, precision, and F1-score on matched objects as follows:

$$\text{Accuracy} = \frac{TP + TN}{TP + TN + FP + FN} \tag{3}$$

$$\text{Precision} = \frac{TP}{TP + FP} \tag{4}$$

$$\text{Recall} = \frac{TP}{TP + FN} \tag{5}$$

and

$$F1 = \frac{2TP}{2TP + FP + FN} \tag{6}$$

where TP is the number of true positives; TN is the number of true negatives; FP is the number of false positives; and FN is the number of false negatives. Segmentation performance metrics were measured per each class, where metrics were computed separately for segmented midpieces and heads. The overall performance of our model was calculated by micro- averaging the results of both classes. Micro-averaging is preferred for datasets with class imbalances, as is in our case, because midpieces are more represented than heads. We selected the model based on the overall F1-score, because our objective was to optimize the model both for precision and recall. Midpieces smaller than 100 pixels and heads smaller than 50 pixels were not used in the evaluation; the object size filter was estimated from the manually annotated images.

Phasor analysis

FLIM images were analyzed using in-house developed TTTR Data Analysis software (written by A. Benda). First, FLIM images displaying average photon arrival times after excitation as a rainbow colormap weighted by the pixel intensity were generated from the raw data (PicoQuant's ptu files) and exported as RGB images (tiff files).

After manual and automatic segmentations the masks were batch loaded back to TTTR software and paired with the original images for object-based analysis. We chose the phasor approach [46, 58] to analyze FLIM images, as this analysis does not assume a priori any model needed for standard fitting of the fluorescence lifetime data, thus eliminating any biases that can come when an inappropriate fit model is used. Standard phasor analysis yields pixel-based plots specific to fluorophores and cells studied. NAD(P)H images of spermatozoa have rather low signal, which makes pixel-based phasor analysis unsuitable for spotting small differences between samples. We instead used object-based phasor approach, in which the signal is first summed up for all pixels in every detected object individually, and the phasor transformation is performed on the excited state decays for whole objects, rather than pixels. To do this, we used the fast Fourier transform algorithm and transformed the excited state decay (TCSPC histogram) of each segmented object in the FLIM image to a point in a two-dimensional (2D) histogram (phasor plot). The phasor coordinates were calculated as previously described [58] using the following equations:

$$g_{i,j}(\omega) = \frac{\int_0^\infty I(t) \bullet cos(\omega t)dt}{\int_0^\infty I(t)dt} \tag{7}$$

and

$$s_{i,j}(\omega) = \frac{\int_0^\infty I(t) \bullet sin(\omega t)dt}{\int_0^\infty I(t)dt} \tag{8}$$

where $g_{i,j}(\omega)$ and $s_{i,j}(\omega)$ represent the x and y coordinates of the phasor plot, respectively, and $I(t)$ is the time-resolved signal, ω is the laser frequency; $\omega = (2\pi f)$, where f is the laser repetition rate, set to 80 MHz in our measurements. The fast Fourier transformations assign a position within the semicircle in phasor plot to each data point, dependent on the fluorescence lifetime of the components (i.e., NAD(P)H) present in the sample. In general, if the lifetime decay is mono-exponential, it appears on the semicircle, whereas multi-exponential decays appear inside the semicircle. We used coumarin-6 solution in ethanol with a mono-exponential decay time as the calibration standard. All FLIM images converted to phasor plots were referenced using the calibration standard measured during each experiment as recommended [111].

Statistics

All statistical tests were performed in R studio software [112] for Mac OSX. The g coordinate phasor values shown to be the most sensitive to free/bound NAD(P)H [46] were used to compare significance among groups across all experiments. First, data were tested for normality (Gaussian distribution) using the Shapiro-Walk test and the homogeneity of variances with Levene's test. When data met both assumptions that is normal distribution with equal variances, linear model (lm) was used as in Figs. 3C, 4, 5B (midpiece), 6A, B, and Additional files 4–9: Figs. S4, S5, S6B, C (head), S8A, B, and S9A, B. When groups of more than two were compared, we followed the general recommendation to use lm followed by Tukey's multiple comparisons post-hoc test as in Fig. 4B and C. Tukey's test is preferred for pairwise comparisons because it increases the likelihood of detecting true differences between groups [113]. When data were non-normally distributed with equal variances, Wilcoxon rank sum test was performed as in Fig. 3B and Additional file 9: Fig. S9C, D (head). When data were normally distributed with unequal variances, generalized least squares method (gls) was used in Fig. 5B (sperm), 6C, D, and Additional files: Fig. S6B, C (principal piece) and S8C, D. We performed correlation analysis and computed the Pearson correlation coefficient between phasor g values and male fertility to examine their relationship. The significance level was set to < 0.05, except for correlation tests in which $P \leq 0.025$ was considered significant (Bonferroni correction for two tests). Sample sizes (n) can be found in the figure legends and in Additional data 10, and individual data points are shown in phasor plots and in Additional data 10. Data shown are derived from representative experiments (results were consistent across two or three independent experiments). Details regarding P-values and statistical tests are provided throughout the main text and figures.

Abbreviations

2-DG	2-Deoxyglucose
2P-FLIM	Two-photon fluorescence lifetime imaging microscopy
ATP	Adenosine triphosphate
B6	C57BL/6J (mouse strain)
B6PF1	(B6 × PWD)F1 (mouse hybrid)
C3H	C3H/N (mouse strain)
d	Distance
FAD	Flavin adenine dinucleotide
FLIM	Fluorescence lifetime imaging microscopy
fps	Frames per second
g	The *x* coordinate of the phasor plot
gls	Generalized least squares
HBSS	Hank's balanced salt solution
IoU	Intersection-over-Union
LDH	Lactate dehydrogenase
lm	Linear model
LMPA	Low melting point agarose
M. m.	*Mus musculus* (house mouse)
NAD(P)H	Nicotinamide adenine dinucleotide and its phosphate (combined signal)
OXPHOS	Oxidative phosphorylation (mitochondrial)
$P_{adj.}$	Probability adjusted for multiple testing
PWD	PWD/Ph (mouse strain)
ROS	Reactive oxygen species
ReLU	Rectified linear unit activation function
s	The *y* coordinate of the phasor plot
TCSPC	Time-correlated single photon counting detection

Supplementary Information

The online version contains supplementary material available at https://doi.org/10.1186/s12915-025-02167-1.

Additional file 1: Fig. S1 2P-FLIM imaging set-up can distinguish between the free and bound NADH. The phasor positions of two NADH states measured by 2P-FLIM in solution: free NADH and bound NADH.

Additional file 2: Fig. S2 Schematic of the metabolic imaging workflow designed for mouse sperm. Our method consists of three steps: **1** Isolation of cauda epididymis and subsequent immersion in 1% LMPA hydrogel solution; **2** in situ 2P-FLIM imaging of endogenous autofluorescent NAD(P)H metabolites at 740 nm excitation; **3** segmentation of single spermatozoa and their subcellular structures from FLIM images. Single spermatozoa and principal pieces are manually segmented into objects based on NAD(P)H fluorescence lifetime signal. We used U-Net –a machine-learning tool—for segmentation of sperm midpieces and heads. The resulting segmented objects are analyzed using phasor analysis to generate metabolic fingerprints for each sample. ex, excitation; fl., fluorescence.

Additional file 3: Fig. S3 2P-FLIM imaging of FAD within motile spermatozoa yields a very weak signal except in the midpiece for both FAD's fluorescence intensity (left) and FAD's fluorescence lifetime (right). Scale bar, 20 µm.

Additional file 4: Fig. S4 Metabolic states of immobilized sperm differ significantly compared to motile sperm. Object-based phasor plots display two separate clusters of individual cells (**A**, left) corresponding to immobilized and motile sperm. Plots depicting midpiece compartments (**A**, right) also differed between immobilized and motile compartments. Sperm heads (**B**, left) of immobilized and motile cells are depicted in phasor plots. Phasor plots show distinct positions of principal pieces (**B**, right) in immobilized sperm and motile ones. Individual sperm cells and subcellular compartments were segmented manually.

Additional file 5: Fig. S5 Related to Fig. 4. Similar metabolic fingerprints of sperm heads and principal pieces among three mouse strains derived from closely related subspecies. **A** Representative FLIM images of PWD, B6 and C3H depicting sperm heads and principal piece subcellular compartments, respectively. Metabolic fingerprints for sperm heads (**B**, left; **C**, left) and principal pieces (**B**, right; **C**, right) are similar among these strains. U-Net segmented heads of PWD, B6 and C3H strains. Principal pieces of PWD, B6 and C3H were segmented manually. Scale bar, 20 µm.

Additional file 6: Fig. S6 Related to Fig. 5. NAD(P)H fingerprints of sperm head and principal piece structures overlapped between fertile and subfertile males. **A** Object-based phasor fingerprints of sperm head and principal piece compartments, respectively. Phasor fingerprints of heads (**B**, left; **C**, left) and principal pieces (**B**, right; **C**, right) show overlapping clusters corresponding to PWD and B6PF1 males. U-Net segmented sperm heads of PWD, and B6PF1 from FLIM images. Principal pieces from PWD, and B6PF1 males were segmented manually.

Additional file 7: Fig. S7 Related to Fig. 5. Overlap in NAD(P)H *g* values between PWD and B6PF1 sperm midpieces.

Additional file 8: Fig. S8 Related to Fig. 6. Metabolic fingerprints of sperm head and principal piece structures in young and old males. The fingerprints of heads **A** (left), **B** (left) were different, but the fingerprints of principal pieces **A** (right), **B** (right) occupy similar positions in phasor plots despite the male age. U-Net segmented sperm heads of old, and young males from FLIM images. Principal pieces from old and young males were segmented manually. H_2O_2 treatment did not change metabolic fingerprints of head **C** (left), **D** (left) and principal pieces **C** (right), **D** (right) when compared to controls. U-Net segmented heads of H_2O_2–treated, and control sperm. Manual segmentation was used for principal pieces from H_2O_2–treated and control sperm.

Additional file 9: Fig. S9. Altered metabolic signatures of spermatozoa due to inhibition of glycolysis. (**A**, **B**) In contrast to PWD control sperm, cells treated with glycolysis inhibitor 2-DG displayed lower mean *g* values of NAD(P)H fingerprints for single spermatozoa, for the midpiece, and higher mean *g* values for the site of glycolysis, but similar *g* values for the sperm heads **C**, **D** (left). Sperm cell segmentations from 2-DG–treated, and control males were generated manually. U-Net segmented: 2-DG midpieces and heads, as well as control midpieces and heads. Principal pieces from 2-DG–treated and control sperm were segmented manually.

Additional file 10: Data underlying all figures.

Acknowledgements
The authors thank Dr. Radek Machan for expert technical assistance in establishing acquisition parameters for FLIM, workers of the Animal Facility of the Institute of Molecular Genetics for mouse keeping, and Dr. Sarka Takacova for English editing.

Authors' contributions
FK and ZT conceived the study. FK designed and performed all experiments, annotated FLIM images, analyzed the data, prepared the figures, and wrote the manuscript. ZT organized mouse crosses. LB adapted U-Net for automated segmentation of sperm from FLIM images and calculated the performance metrics of the network. DP setup FLIM imaging, measured laser power, and calibrated the instrument prior to each experiment. AB developed the custom-written TTTR Data Analysis software for phasor analysis and supervised LB's work. LB, AB, DP, and ZT commented and edited the manuscript. ZT and FK acquired funding and supervised the study. All authors read and approved the final manuscript.

Funding
This work was supported by the Czech Science Foundation (CSF 19-06272S), Czech Academy of Sciences (RVO 68378050), Ministry of Education, Youth and Sports of the Czech Republic (LQ1604 NPUII, LM2023036 CCP, LM2015042 CESNET, LM2023050 Czech BioImaging), and European Regional Development Fund (CZ.1.05/1.1.00/02.0109 BIOCEV, CZ.1.05/2.1.00/19.0395, CZ.02.1.01/0.0/0.0/16_013/0001775).

Data availability
All data generated or analysed during this study are included in this published article, its supplementary information files and publicly available repositories. The supporting data underlying all figures are presented in Additional file 10. The phasor analysis software for FLIM data via Time-Tagged Time-Resolved raw image is available on https://github.com/BendaAles/TTTR-Data-Analysis and at https://doi.org/10.5281/zenodo.14754045. The code for the automated sperm segmentation from FLIM images can be found on https://github.com/lenkaback/FLIM-Sperm-Segmentation https://doi.org/10.5281/zenodo.14869563. 2P-FLIM images of sperm with manual masks can be found on https://doi.org/10.5281/zenodo.14006097. Any additional information is available from the corresponding authors upon request.

Declarations

Ethics approval and consent to participate
All animal experiments were approved by the Ethics Committee for the Work with Animals of the Institute of Molecular Genetics, Prague (permits Nos. 9/2016 and 16/2019).

Consent for publication
Not applicable.

Competing interests
The authors declare that they have no competing interests.

Received: 19 April 2024 Accepted: 17 February 2025
Published online: 24 March 2025

References

1. Zecchin A, Stapor PC, Goveia J, Carmeliet P. Metabolic pathway compartmentalization: an underappreciated opportunity? Curr Opin Biotechnol. 2015;34:73–81.

2. Lindemann CB, Lesich KA. Functional anatomy of the mammalian sperm flagellum. Cytoskeleton (Hoboken). 2016;73(11):652–69.
3. Freitas MJ, Vijayaraghavan S, Fardilha M. Signaling mechanisms in mammalian sperm motility. Biol Reprod. 2017;96(1):2–12.
4. Ford WC. Glycolysis and sperm motility: does a spoonful of sugar help the flagellum go round? Hum Reprod Update. 2006;12(3):269–74.
5. du Plessis SS, Agarwal A, Mohanty G, van der Linde M. Oxidative phosphorylation versus glycolysis: what fuel do spermatozoa use? Asian J Androl. 2015;17(2):230–5.
6. Alves LQ, Ruivo R, Valente R, Fonseca MM, Machado AM, Plon S, Monteiro N, Garcia-Parraga D, Ruiz-Diaz S, Sanchez-Calabuig MJ, et al. A drastic shift in the energetic landscape of toothed whale sperm cells. Curr Biol. 2021;31(16):3648–3655 e3649.
7. Fraser LR, Quinn PJ. A glycolytic product is obligatory for initiation of the sperm acrosome reaction and whiplash motility required for fertilization in the mouse. J Reprod Fertil. 1981;61(1):25–35.
8. Bone W, Jones NG, Kamp G, Yeung CH, Cooper TG. Effect of ornidazole on fertility of male rats: inhibition of a glycolysis-related motility pattern and zona binding required for fertilization in vitro. J Reprod Fertil. 2000;118(1):127–35.
9. Hoshi K, Tsukikawa S, Sato A. Importance of Ca2+, K+ and glucose in the medium for sperm penetration through the human zona pellucida. Tohoku J Exp Med. 1991;165(2):99–104.
10. Williams AC, Ford WC. The role of glucose in supporting motility and capacitation in human spermatozoa. J Androl. 2001;22(4):680–95.
11. Demain LA, Conway GS, Newman WG. Genetics of mitochondrial dysfunction and infertility. Clin Genet. 2017;91(2):199–207.
12. Folgero T, Bertheussen K, Lindal S, Torbergsen T, Oian P. Mitochondrial disease and reduced sperm motility. Hum Reprod. 1993;8(11):1863–8.
13. Carra E, Sangiorgi D, Gattuccio F, Rinaldi AM. Male infertility and mitochondrial DNA. Biochem Biophys Res Commun. 2004;322(1):333–9.
14. Nakada K, Sato A, Yoshida K, Morita T, Tanaka H, Inoue S, Yonekawa H, Hayashi J. Mitochondria-related male infertility. Proc Natl Acad Sci U S A. 2006;103(41):15148–53.
15. Jiang M, Kauppila TES, Motori E, Li X, Atanassov I, Folz-Donahue K, Bonekamp NA, Albarran-Gutierrez S, Stewart JB, Larsson NG. Increased total mtDNA copy number cures male infertility despite unaltered mtDNA mutation load. Cell Metab. 2017;26(2):429–436 e424.
16. Rovio AT, Marchington DR, Donat S, Schuppe HC, Abel J, Fritsche E, Elliott DJ, Laippala P, Ahola AL, McNay D, et al. Mutations at the mitochondrial DNA polymerase (POLG) locus associated with male infertility. Nat Genet. 2001;29(3):261–2.
17. Trifunovic A, Wredenberg A, Falkenberg M, Spelbrink JN, Rovio AT, Bruder CE, Bohlooly YM, Gidlof S, Oldfors A, Wibom R, et al. Premature ageing in mice expressing defective mitochondrial DNA polymerase. Nature. 2004;429(6990):417–23.
18. Takasaki N, Tachibana K, Ogasawara S, Matsuzaki H, Hagiuda J, Ishikawa H, Mochida K, Inoue K, Ogonuki N, Ogura A, et al. A heterozygous mutation of GALNTL5 affects male infertility with impairment of sperm motility. Proc Natl Acad Sci U S A. 2014;111(3):1120–5.
19. Liu X, Li Q, Wang W, Liu F. Aberrant expression of spermspecific glycolytic enzymes are associated with poor sperm quality. Mol Med Rep. 2019;19(4):2471–8.
20. Miki K, Qu W, Goulding EH, Willis WD, Bunch DO, Strader LF, Perreault SD, Eddy EM, O'Brien DA. Glyceraldehyde 3-phosphate dehydrogenase-S, a sperm-specific glycolytic enzyme, is required for sperm motility and male fertility. Proc Natl Acad Sci U S A. 2004;101(47):16501–6.
21. Reynolds S, Calvert SJ, Paley MN, Pacey AA. 1H magnetic resonance spectroscopy of live human sperm. Mol Hum Reprod. 2017;23(7):441–51.
22. Paiva C, Amaral A, Rodriguez M, Canyellas N, Correig X, Ballesca JL, Ramalho-Santos J, Oliva R. Identification of endogenous metabolites in human sperm cells using proton nuclear magnetic resonance ((1) H-NMR) spectroscopy and gas chromatography-mass spectrometry (GC-MS). Andrology. 2015;3(3):496–505.
23. Menezes EB, Velho ALC, Santos F, Dinh T, Kaya A, Topper E, Moura AA, Memili E. Uncovering sperm metabolome to discover biomarkers for bull fertility. BMC Genomics. 2019;20(1):714.
24. Jensen EC. Use of fluorescent probes: their effect on cell biology and limitations. Anat Rec (Hoboken). 2012;295(12):2031–6.
25. Kolenc OI, Quinn KP. Evaluating cell metabolism through autofluorescence imaging of NAD(P)H and FAD. Antioxid Redox Signal. 2019;30(6):875–89.
26. Chance B, Schoener B, Oshino R, Itshak F, Nakase Y. Oxidation-reduction ratio studies of mitochondria in freeze-trapped samples. NADH and flavoprotein fluorescence signals. J Biol Chem. 1979;254(11):4764–71.
27. Patterson GH, Knobel SM, Arkhammar P, Thastrup O, Piston DW. Separation of the glucose-stimulated cytoplasmic and mitochondrial NAD(P) H responses in pancreatic islet beta cells. Proc Natl Acad Sci U S A. 2000;97(10):5203–7.
28. Huang S, Heikal AA, Webb WW. Two-photon fluorescence spectroscopy and microscopy of NAD(P)H and flavoprotein. Biophys J. 2002;82(5):2811–25.
29. Blinova K, Levine RL, Boja ES, Griffiths GL, Shi ZD, Ruddy B, Balaban RS. Mitochondrial NADH fluorescence is enhanced by complex I binding. Biochemistry. 2008;47(36):9636–45.
30. Skala MC, Riching KM, Gendron-Fitzpatrick A, Eickhoff J, Eliceiri KW, White JG, Ramanujam N. In vivo multiphoton microscopy of NADH and FAD redox states, fluorescence lifetimes, and cellular morphology in precancerous epithelia. Proc Natl Acad Sci U S A. 2007;104(49):19494–9.
31. Georgakoudi I, Quinn KP. Optical imaging using endogenous contrast to assess metabolic state. Annu Rev Biomed Eng. 2012;14:351–67.
32. Georgakoudi I, Quinn KP. Label-free optical metabolic imaging in cells and tissues. Annu Rev Biomed Eng. 2023;25:413–43.
33. Lakowicz JR, Szmacinski H, Nowaczyk K, Johnson ML. Fluorescence lifetime imaging of free and protein-bound NADH. Proc Natl Acad Sci U S A. 1992;89(4):1271–5.
34. Berezin MY, Achilefu S. Fluorescence lifetime measurements and biological imaging. Chem Rev. 2010;110(5):2641–84.
35. Sparks H, Kondo H, Hooper S, Munro I, Kennedy G, Dunsby C, French P, Sahai E. Heterogeneity in tumor chromatin-doxorubicin binding revealed by in vivo fluorescence lifetime imaging confocal endomicroscopy. Nat Commun. 2018;9(1):2662.
36. Becker W, Bergmann A, Hink MA, Konig K, Benndorf K, Biskup C. Fluorescence lifetime imaging by time-correlated single-photon counting. Microsc Res Tech. 2004;63(1):58–66.
37. Becker W. Fluorescence lifetime imaging–techniques and applications. J Microsc. 2012;247(2):119–36.
38. Datta R, Heaster TM, Sharick JT, Gillette AA, Skala MC. Fluorescence lifetime imaging microscopy: fundamentals and advances in instrumentation, analysis, and applications. J Biomed Opt. 2020;25(7):1–43.
39. Serafino MJ, Jo JA. Direct frequency domain fluorescence lifetime imaging using simultaneous ultraviolet and visible excitation. Biomed Opt Express. 2023;14(4):1608–25.
40. Konig K, So PT, Mantulin WW, Tromberg BJ, Gratton E. Two-photon excited lifetime imaging of autofluorescence in cells during UVA and NIR photostress. J Microsc. 1996;183(Pt 3):197–204.
41. Pattison DI, Davies MJ. Actions of ultraviolet light on cellular structures. EXS. 2006;96:131–57.
42. Park J, Gao L. Advancements in fluorescence lifetime imaging microscopy Instrumentation: towards high speed and 3D. Curr Opin Solid State Mater Sci. 2024;30:30.
43. Sorrells JE, Iyer RR, Yang L, Bower AJ, Spillman DR Jr, Chaney EJ, Tu H, Boppart SA. Real-time pixelwise phasor analysis for video-rate two-photon fluorescence lifetime imaging microscopy. Biomed Opt Express. 2021;12(7):4003–19.
44. Samimi K, Desa DE, Lin W, Weiss K, Li J, Huisken J, Miskolci V, Huttenlocher A, Chacko JV, Velten A, et al. Light-sheet autofluorescence lifetime imaging with a single-photon avalanche diode array. J Biomed Opt. 2023;28(6): 066502.
45. Moen E, Bannon D, Kudo T, Graf W, Covert M, Van Valen D. Deep learning for cellular image analysis. Nat Methods. 2019;16(12):1233–46.
46. Stringari C, Cinquin A, Cinquin O, Digman MA, Donovan PJ, Gratton E. Phasor approach to fluorescence lifetime microscopy distinguishes different metabolic states of germ cells in a live tissue. Proc Natl Acad Sci U S A. 2011;108(33):13582–7.
47. Wetzker C, Reinhardt K. Distinct metabolic profiles in Drosophila sperm and somatic tissues revealed by two-photon NAD(P)H and FAD autofluorescence lifetime imaging. Sci Rep. 2019;9(1):19534.
48. Reinhardt K, Breunig HG, Uchugonova A, Konig K. Sperm metabolism is altered during storage by female insects: evidence from two-photon

autofluorescence lifetime measurements in bedbugs. J R Soc Interface. 2015;12(110):0609.
49. Vishnyakova P, Nikonova E, Jumaniyazova E, Solovyev I, Kirillova A, Farmakovskaya M, Savitsky A, Shirshin E, Sukhikh G, Fatkhudinov T. Fluorescence lifetime imaging microscopy as an instrument for human sperm assessment. Biochem Biophys Res Commun. 2023;645:10–6.
50. Cong A, Pimenta RML, Lee HB, Mereddy V, Holy J, Heikal AA. Two-photon fluorescence lifetime imaging of intrinsic NADH in three-dimensional tumor models. Cytometry A. 2019;95(1):80–92.
51. Norambuena A, Wallrabe H, Cao R, Wang DB, Silva A, Svindrych Z, Periasamy A, Hu S, Tanzi RE, Kim DY et al. A novel lysosome-to-mitochondria signaling pathway disrupted by amyloid- b oligomers. EMBO J. 2018;37(22):1–18.
52. Aguilar-Arnal L, Ranjit S, Stringari C, Orozco-Solis R, Gratton E, Sassone-Corsi P. Spatial dynamics of SIRT1 and the subnuclear distribution of NADH species. Proc Natl Acad Sci U S A. 2016;113(45):12715–20.
53. Wright BK, Andrews LM, Markham J, Jones MR, Stringari C, Digman MA, Gratton E. NADH distribution in live progenitor stem cells by phasor-fluorescence lifetime image microscopy. Biophys J. 2012;103(1):L7–9.
54. Winet H, Bernstein GS, Head J. Observations on the response of human spermatozoa to gravity, boundaries and fluid shear. J Reprod Fertil. 1984;70(2):511–23.
55. Maude AD. Non-random distribution of bull spermatozoa in a drop of sperm suspension. Nature. 1963;200:381.
56. Woolley DM. Motility of spermatozoa at surfaces. Reproduction. 2003;126(2):259–70.
57. Tourmente M, Varea-Sanchez M, Roldan ERS. Faster and more efficient swimming: energy consumption of murine spermatozoa under sperm competitiondagger. Biol Reprod. 2019;100(2):420–8.
58. Digman MA, Caiolfa VR, Zamai M, Gratton E. The phasor approach to fluorescence lifetime imaging analysis. Biophys J. 2008;94(2):L14–16.
59. Nakashima N, Yoshihara K, Tanaka F, Yagi K. Picosecond fluorescence lifetime of the coenzyme of D-amino acid oxidase. J Biol Chem. 1980;255(11):5261–3.
60. Buffone MG, Ijiri TW, Cao W, Merdiushev T, Aghajanian HK, Gerton GL. Heads or tails? Structural events and molecular mechanisms that promote mammalian sperm acrosomal exocytosis and motility. Mol Reprod Dev. 2012;79(1):4–18.
61. Kuang W, Zhang J, Lan Z, Deepak R, Liu C, Ma Z, Cheng L, Zhao X, Meng X, Wang W, et al. SLC22A14 is a mitochondrial riboflavin transporter required for sperm oxidative phosphorylation and male fertility. Cell Rep. 2021;35(3): 109025.
62. Ferramosca A, Zara V. Bioenergetics of mammalian sperm capacitation. Biomed Res Int. 2014;2014: 902953.
63. Orgebin-Crist MC. Sperm maturation in rabbit epididymis. Nature. 1967;216(5117):816–8.
64. Rosenthal N, Brown S. The mouse ascending: perspectives for human-disease models. Nat Cell Biol. 2007;9(9):993–9.
65. Cinco R, Digman MA, Gratton E, Luderer U. Spatial characterization of bioenergetics and metabolism of primordial to preovulatory follicles in whole ex vivo murine ovary. Biol Reprod. 2016;95(6):129.
66. Renaud O, Herbomel P, Kissa K. Studying cell behavior in whole zebrafish embryos by confocal live imaging: application to hematopoietic stem cells. Nat Protoc. 2011;6(12):1897–904.
67. Cao R, Wallrabe H, Periasamy A. Multiphoton FLIM imaging of NAD(P)H and FAD with one excitation wavelength. J Biomed Opt. 2020;25(1):1–16.
68. Ma N, Mochel NR, Pham PD, Yoo TY, Cho KWY, Digman MA. Label-free assessment of pre-implantation embryo quality by the Fluorescence Lifetime Imaging Microscopy (FLIM)-phasor approach. Sci Rep. 2019;9(1):13206.
69. Walsh AJ, Mueller KP, Tweed K, Jones I, Walsh CM, Piscopo NJ, Niemi NM, Pagliarini DJ, Saha K, Skala MC. Classification of T-cell activation via autofluorescence lifetime imaging. Nat Biomed Eng. 2021;5(1):77–88.
70. Stringari C, Wang H, Geyfman M, Crosignani V, Kumar V, Takahashi JS, Andersen B, Gratton E. In vivo single-cell detection of metabolic oscillations in stem cells. Cell Rep. 2015;10(1):1–7.
71. Olaf Ronneberger PF, Thomas Brox: U-Net: convolutional networks for biomedical image segmentation. 2015. Preprint at: https://arxiv.org/abs/1505.04597.
72. Tourmente M, Rowe M, Gonzalez-Barroso MM, Rial E, Gomendio M, Roldan ER. Postcopulatory sexual selection increases ATP content in rodent spermatozoa. Evolution. 2013;67(6):1838–46.
73. Tourmente M, Villar-Moya P, Rial E, Roldan ER. Differences in ATP generation via glycolysis and oxidative phosphorylation and relationships with sperm motility in mouse species. J Biol Chem. 2015;290(33):20613–26.
74. Tourmente M, Villar-Moya P, Varea-Sanchez M, Luque-Larena JJ, Rial E, Roldan ER. Performance of rodent spermatozoa over time is enhanced by increased ATP concentrations: the role of sperm competition. Biol Reprod. 2015;93(3):64.
75. Albrechtova J, Albrecht T, Dureje L, Pallazola VA, Pialek J. Sperm morphology in two house mouse subspecies: do wild-derived strains and wild mice tell the same story? PLoS ONE. 2014;9(12): e115669.
76. Gage MJ, Macfarlane CP, Yeates S, Ward RG, Searle JB, Parker GA. Spermatozoal traits and sperm competition in Atlantic salmon: relative sperm velocity is the primary determinant of fertilization success. Curr Biol. 2004;14(1):44–7.
77. Birkhead TR, Martinez JG, Burke T, Froman DP. Sperm mobility determines the outcome of sperm competition in the domestic fowl. Proc Biol Sci. 1999;266(1430):1759–64.
78. Kahrl AF, Snook RR, Fitzpatrick JL. Fertilization mode differentially impacts the evolution of vertebrate sperm components. Nat Commun. 2022;13(1):6809.
79. Samplaski MK, Nangia AK. Adverse effects of common medications on male fertility. Nat Rev Urol. 2015;12(7):401–13.
80. Sakkas D, Ramalingam M, Garrido N, Barratt CL. Sperm selection in natural conception: what can we learn from Mother Nature to improve assisted reproduction outcomes? Hum Reprod Update. 2015;21(6):711–26.
81. Leung ETY, Lee CL, Tian X, Lam KKW, Li RHW, Ng EHY, Yeung WSB, Chiu PCN. Simulating nature in sperm selection for assisted reproduction. Nat Rev Urol. 2022;19(1):16–36.
82. Kusari F, Mihola O, Schimenti J, Trachtulec Z. Meiotic Epigenetic Factor PRDM9 Impacts Sperm Quality of Hybrid Mice. Reprod. 2020;160(1):53–64.
83. Mihola O, Kobets T, Krivankova K, Linhartova E, Gasic S, Schimenti JC, Trachtulec Z. Copy-number variation introduced by long transgenes compromises mouse male fertility independently of pachytene checkpoints. Chromosoma. 2020;129(1):69–82.
84. Sun N, Youle RJ, Finkel T. The mitochondrial basis of aging. Mol Cell. 2016;61(5):654–66.
85. Lopez-Otin C, Blasco MA, Partridge L, Serrano M, Kroemer G. The hallmarks of aging. Cell. 2013;153(6):1194–217.
86. Aitken RJ. Impact of oxidative stress on male and female germ cells: implications for fertility. Reproduction. 2020;159(4):R189–201.
87. He L, He T, Farrar S, Ji L, Liu T, Ma X. Antioxidants maintain cellular redox homeostasis by elimination of reactive oxygen species. Cell Physiol Biochem. 2017;44(2):532–53.
88. Twigg J, Fulton N, Gomez E, Irvine DS, Aitken RJ. Analysis of the impact of intracellular reactive oxygen species generation on the structural and functional integrity of human spermatozoa: lipid peroxidation, DNA fragmentation and effectiveness of antioxidants. Hum Reprod. 1998;13(6):1429–36.
89. Almeida S, Rato L, Sousa M, Alves MG, Oliveira PF. Fertility and sperm quality in the aging male. Curr Pharm Des. 2017;23(30):4429–37.
90. Selvaratnam J, Robaire B. Overexpression of catalase in mice reduces age-related oxidative stress and maintains sperm production. Exp Gerontol. 2016;84:12–20.
91. Ozkosem B, Feinstein SI, Fisher AB, O'Flaherty C. Advancing age increases sperm chromatin damage and impairs fertility in peroxiredoxin 6 null mice. Redox Biol. 2015;5:15–23.
92. Paoli D, Pecora G, Pallotti F, Faja F, Pelloni M, Lenzi A, Lombardo F. Cytological and molecular aspects of the ageing sperm. Hum Reprod. 2019;34(2):218–27.
93. Cocuzza M, Athayde KS, Agarwal A, Sharma R, Pagani R, Lucon AM, Srougi M, Hallak J. Age-related increase of reactive oxygen species in neat semen in healthy fertile men. Urology. 2008;71(3):490–4.
94. Iaffaldano N, Di Iorio M, Mannina L, Paventi G, Rosato MP, Cerolini S, Sobolev AP. Age-dependent changes in metabolic profile of turkey spermatozoa as assessed by NMR analysis. PLoS ONE. 2018;13(3): e0194219.

95. Losano J, Angrimani D, Dalmazzo A, Rui BR, Brito MM, Mendes CM, Kawai G, Vannucchi CI, Assumpcao M, Barnabe VH, et al. Effect of mitochondrial uncoupling and glycolysis inhibition on ram sperm functionality. Reprod Domest Anim. 2017;52(2):289–97.
96. Saggiorato G, Alvarez L, Jikeli JF, Kaupp UB, Gompper G, Elgeti J. Human sperm steer with second harmonics of the flagellar beat. Nat Commun. 2017;8(1):1415.
97. Becker W, Braun L, Suarez-Ibarrol R, Miernik A. Metabolic IMAGING BY SIMULTANEous FLIM of NAD(P)H and FAD. Current Directions in Biomedical Engineering. 2020;6(3):254–6.
98. Gregorova S, Forejt J. PWD/Ph and PWK/Ph inbred mouse strains of Mus m. musculus subspecies–a valuable resource of phenotypic variations and genomic polymorphisms. Folia Biol (Praha). 2000;46(1):31–41.
99. Sun Y, Day RN, Periasamy A. Investigating protein-protein interactions in living cells using fluorescence lifetime imaging microscopy. Nat Protoc. 2011;6(9):1324–40.
100. Durmaz AR, Muller M, Lei B, Thomas A, Britz D, Holm EA, Eberl C, Mucklich F, Gumbsch P. A deep learning approach for complex microstructure inference. Nat Commun. 2021;12(1):6272.
101. Pan C, Schoppe O, Parra-Damas A, Cai R, Todorov MI, Gondi G, von Neubeck B, Bogurcu-Seidel N, Seidel S, Sleiman K, et al. Deep learning reveals cancer metastasis and therapeutic antibody targeting in the entire body. Cell. 2019;179(7):1661–1676 e1619.
102. Nygate YN, Levi M, Mirsky SK, Turko NA, Rubin M, Barnea I, Dardikman-Yoffe G, Haifler M, Shalev A, Shaked NT. Holographic virtual staining of individual biological cells. Proc Natl Acad Sci U S A. 2020;117(17):9223–31.
103. Manifold B, Men S, Hu R, Fu D. A versatile deep learning architecture for classification and label-free prediction of hyperspectral images. Nat Mach Intell. 2021;3:306–15.
104. Glastonbury CA, Pulit SL, Honecker J, Censin JC, Laber S, Yaghootkar H, Rahmioglu N, Pastel E, Kos K, Pitt A, et al. Machine learning based histology phenotyping to investigate the epidemiologic and genetic basis of adipocyte morphology and cardiometabolic traits. PLoS Comput Biol. 2020;16(8): e1008044.
105. Kingma DP, Ba J: Adam: a method for stochastic optimization. 2014. Preprint at: https://arxiv.org/abs/1412.6980.
106. He K, Zhang X, Ren S, Sun J: Delving deep into rectifiers: surpassing human-level performance on ImageNet classification. IEEE International Conference on Computer Vision (ICCV). 2015:1026-1034.
107. Abadi M. TensorFlow: learning functions at scale. ACM SIGPLAN Notices. 2016;51(9):1–1.
108. Kuhn HW: The Hungarian method for the assignment problem. Naval research logistics quarterly. 1955.
109. Soltanian-Zadeh S, Sahingur K, Blau S, Gong Y, Farsiu S. Fast and robust active neuron segmentation in two-photon calcium imaging using spatiotemporal deep learning. Proc Natl Acad Sci U S A. 2019;116(17):8554–63.
110. Giovannucci A, Friedrich J, Gunn P, Kalfon J, Brown BL, Koay SA, Taxidis J, Najafi F, Gauthier JL, Zhou P, et al. CaImAn an open source tool for scalable calcium imaging data analysis. Elife. 2019;8:8.
111. Ranjit S, Malacrida L, Jameson DM, Gratton E. Fit-free analysis of fluorescence lifetime imaging data using the phasor approach. Nat Protoc. 2018;13(9):1979–2004.
112. R Development Core Team. R: a language and environment for statistical computing. Vienna, Austria: R Foundation for Statistical Computing; 2019.
113. Midway S, Robertson M, Flinn S, Kaller M. Comparing multiple comparisons: practical guidance for choosing the best multiple comparisons test. PeerJ. 2020;8: e10387.

Publisher's Note